TURUN YLIOPISTO

3D-modelling of microfracture networks associated with faulting in the crystalline Wiborg rapakivi granite

Mathias Lauraeus

Geology

Master's Thesis

Scope: 30 ECTS

Supervisor:

Pietari Skyttä

18.11.2021

Turku

University of Turku

Department of Geography and Geology, Geology section

LAURAEUS, MATHIAS: 3D-modelling of microfracture networks associated with faulting in the crystalline Wiborg rapakivi granite

MSc thesis, 43 p + 1 appendix.

Bedrock geology

November 2021

The originality of this thesis has been checked in accordance with the University of Turku quality assurance system using the Turnitin OriginalityCheck service.

The main purpose of this MSc thesis is to study the 3D geometry of secondary microfractures associated with faults by using grinding the tomography method. Information on the 3D geometry of microfractures can be used, for example, for predicting the hydraulic conductivity of rocks and for more accurate interpretation of generation mechanisms and kinematics of faults. A 3D model of a microfracture network of one oriented rock sample was constructed from data collected with grinding tomography methods. The interpretations made on the 3D model were compared with the field measurements and GIS fracture trace interpretations based on 2D orthophotography data collected with a drone and a digital SLR camera. The second purpose of this thesis was to compare these two scales of 2D fracture trace datasets and find out how the change of observation scale from meters to centimeters affects the 2D topology and orientation distribution of the fracture networks. The study area is located on the Island of Orrengrund, Loviisa, SW Finland. The fault studied in the thesis is a sinistral strike-slip fault with a vertical dip, and a N-S trend.

In the grinding tomography method used in this thesis, a cylindrical 50*50*50 mm sample of rock is glued on a glass plate and grinded in slices with a 3D-grinder, so that after each slice the machine takes an image of the surface of the sample. When the images are combined by knowing the vertical position of each image, interpretations can be made on the observed fractures, and a 3D model can be constructed. In this thesis, a new GRN16 3D grinder of the University of Turku geology section was used.

Grinding tomography images of the oriented rock sample were georeferenced on the orthophotos with QGIS software, so that the orientation data obtained from the 3D model of microfracture network was comparable with 2D fracture trace data and field measurements.

The results of the thesis showed that the 3D model of microfracture network constructed using grinding tomography has almost perfect correlation with the orientation distribution and cross-cut relationships of field measurements. The study also revealed that the new 3D grinder of the University of Turku geology Section solves numerous problems regarding the use of the grinding tomography method in geosciences. In addition, topological differences were observed between the two different-scale 2D fracture trace datasets, reflecting that the topological properties of the fault's fracture systems could be scale-dependent.

Keywords: fault, damage zone, fracture, microfracture, fracture network, 3D-modelling, topology.

Turun yliopisto

Maantieteen ja geologian laitos, geologian osasto

LAURAEUS, MATHIAS: 3D-modelling of microfracture networks associated with faulting in the crystalline Wiborg rapakivi granite

Pro gradu -tutkielma, 43 p + 1 liite.

Kallioperägeologia

Marraskuu 2021

Turun yliopiston laatujärjestelmän mukaisesti tämän julkaisun alkuperäisyys on tarkastettu Turnitin Originality Check -järjestelmällä.

Tämän Pro gradu -tutkielman päätarkoituksena oli tutkia kallioperän siirroksiin liittyvän sekundäärisen mikrorakoilun 3D-geometriaa hiontatomografiamenetelmällä. Tietoa mikrorakoilun 3D-geometriasta voidaan käyttää esimerkiksi kivien vedenjohtavuuden ennustamiseen sekä siirrosten syntymekanismien ja kinematiikan tarkemmassa tulkinnassa. Hiontatomografiamenetelmällä kerätystä aineistosta rakennettiin yhden suunnatun kivinäytteen mikrorakoverkon 3D-malli. 3D-mallista tehtyjä tulkintoja verrattiin dronella sekä järjestelmäkameralla kerätyn 2D-ortokuva-aineiston GIS-rakotulkintoihin, sekä maastossa tehtyihin mittaustuloksiin. Työn toisena tarkoituksena oli vertailla näitä kahden eri mittakaavan 2D-rakotulkintaa, ja tutkia miten tarkastelumittakaavan pienentäminen metreistä sentteihin vaikuttaa rakoverkon 2D-topologiaan ja -suuntajakaumaan. Tutkimusalue sijaitsee Orrengrundin saarella, Loviisan edustalla. Tutkielmassa tutkittu siirros on vasenkätinen. likimain pystyasentoinen kulkusiirros, jonka kulku on pohjois-etelä -suuntainen.

Tässä työssä käytetyssä hiontatomografiamenetelmässä sylinterin muotoinen 50*50*50 mm kivinäyte liimattiinn lasilevylle, ja hiottiin 3D-hiomakoneella siten, että jokaisen hiotun viipaleen jälkeen kone otti valokuvan näytteen pinnasta. Kun valokuvat yhdistetään, niissä näkyvästä rakoverkosta voidaan tehdä rakotulkintoja, ja rakentaa 3D-malli. Tässä työssä käytettiin Turun yliopiston geologian laitoksen uutta GRN16 3D-hiomakonetta.

Suunnatun kivinäytteen hiontatomografiakuvat georeferoitiin suunnaltaan ja sijainniltaan ortokuvien päälle QGIS-paikkatieto-ohjelmistolla, jolloin mikrorakoverkon 3D-mallista saatu suunta-aineisto oli vertailukelpoista ortokuvista tehtyihin 2D-rakotulkintoihin sekä paljastumamittauksiin.

Tutkielman tulokset osoittivat, että hiontatomografiamenetelmän aineistolla rakennettu mikrorakoverkkoa kuvaava 3D-malli korreloi lähes täydellisesti suuntajakaumaltaan ja leikkaussuhteiltaan siirroksesta tehtyihin paljastumamittauksiin. Tutkimuksessa myös selvisi, että Turun yliopiston geologian osaston uusi 3D-hiomakone korjaa lukuisia ongelmia, jotka liittyvät hiontatomografiamenetelmän käyttöön geotieteissä. Kahden eri mittakaavaisen 2D-rakotulkinta-aineiston välillä puolestaan havaittiin topologisia eroavaisuuksia, jotka viittaavat siirroksen rakosysteemin topologisten ominaisuuksien olevan mittakaavasta riippuvaisia.

Avainsanat: siirros, tuhovyöhyke, rako, mikrorako, rakoverkko, 3D-mallinnus, topologia.

Contents

1. Introduction

Understanding fractures in rocks is essential for both science and practical applications within engineering. Of particular significance are the secondary fractures, which are associated with faults, and can hence aid in constraining their properties and histories (Kranz, 1983; Bastesen and Rotevatn, 2012). Due to the morphological similarities between cracks, joints, and faults, the comparisons between different fracture data can be also applied to solve geophysical scalability problems (Kranz, 1983). From an engineering point of view, the propagation and interaction of fractures in microscopic-scale is significant from the perspective of the stability of underground openings (Nasseri et al. 2011) and potential fluid flow pathways in fractured crystalline rocks (Suzuki et al., 1969; Nasseri et. al 2011). Moreover, in the underground nuclear waste repository facilities such as the Olkiluoto in Finland, the 3D-dimensional fracture systems have a risk of making pathways for radionuclides to be transported with groundwater (Fox et al., 2012).

Classification and definition of secondary fracturing have been extensively discussed by e.g. Kim et al. (2004), Peacock et al. (2017), and Choi et al. (2016). As far as these studies give generalized models about the 3D distribution of fault-related damage, the observation and resulting ideas are dominantly 2-dimensional in character (Choi et al., 2016). The reason for this is derived from the limitations to study the 3D-architecture of the fracture networks; interpretations of 3D-geometry of fractures are usually made on individual 2-dimensional exposure surfaces (Peacock et al., 2017). Since the faults and related damage zones are three-dimensional complex volumes with a variety of internal structures (Choi et al., 2016), the existing 2D-driven models have a lot of uncertainties.

Some research on secondary fractures has been conducted in three dimensions, such as the geomechanical models of Crider and Pollard (1998) and Martel et al. (2001), which describe the local stress perturbations and mechanical interactions associated with the development of secondary faults. By contrast, Martel and Boger (1998) have addressed the “geometry and mechanics of secondary fracturing around small three-dimensional faults in granitic rock” through field measurements that complement the mechanical modelling. Laboratory-based modelling apoproaches have been used e.g. by Nasseri et al. (2011), who used x-ray microtomography methods to model the generation of small-scale secondary fractures in anisotropic granite. Even though the numerical methods (e.g. Crider and Pollard, 1998; Martel and Boger, 1998; Maerten, Gillespie and Pollard, 2002) and laboratory experiments (e.g. Nasseri et al. 2011) may be useful for correlations with the naturally occurring brittle structures, the lack of detailed 3D-models over brittle fractures in nature rarely allow such correlations, with particular reference to samples which geological setting is adequately characterized. For instance, strike orientations of secondary fractures and their topological

relationship to the faults have been discussed in various articles (e.g. Sanderson and Peacock 2020; Peacock et al. 2018; Sanderson and Nixon 2015; Martel and Boger 1998; Kranz 1983; Tchalenko 1970) but information about characteristic dip-angles of the secondary fractures is seldomly found in the literature. In this sense, the development of theories requires more sophisticated 3D models over the secondary fracture patterns.

In this thesis, a new methodology is introduced for detailed modelling of 3D geometry of secondary microfracturing associated with faults. The methodology utilizes an automatized 3D-grinding tomography imagery data taken with a recently developed 3D-grinder at the University of Turku, which solves multiple existing problems concerning the conduction of grinding tomography experiments. Interpretation of the tomography models is aided by a comprehensive geological background consisting of high-resolution 2D fracture trace analysis, joint measurements, and field observations, which are used for linkage between the regional structures and the 3D-tomography modelling results. The utilization of these models aims at an improved understanding about the properties of the small-scale fracture networks (e.g. dips, orientations and networking of the secondary fractures). Consequently, the results can be used to understand the kinematic character of brittle faults and hydrological properties of contrasting rock types. In the 2D analysis of the fracture networks within the study area, the project applies the methodology of scalability and topology analysis methodology for fracture trace networks used in the KARIKKO-project of the Geological Survey of Finland and aims to refine the observation scale from meter-scale (UAV-scale = drone-scale) to centimetre-scale (SLR-camera-scale).

One oriented 50*50*50 mm 3D sample from a sinistral brittle strike-slip fault is studied in this thesis. The study site is located within mesoscopically homogenous 1.65-1.62 Ga Wiborg rapakivi granite batholith (Vaasjoki, et al. 1991; Rämö and Haapala, 1995), which has not undergone the complex Svecofennian ~1.8 Ga orogenic evolution (e.g. Nironen, 1997). Consequently, the target of the study is optimal to understand the primary processes related to early stages of faulting as there is no need to consider structural inheritances form older ductile structures. In addition to the optimal rock type, the Orrengrund Island and the archipelago of Southern Finland in general, have extensively exposed glacially polished outcrops, from which the high-resolution UAV- and SLR-photogrammetry can be obtained for the purposes of e.g. GIS fracture trace interpretations (remote mapping).

2. Geological background

2.1. Post-svecofennian brittle structures in Southern Finland

Recent developments in understanding the brittle structural evolution in Southern Finland is tightly associated with studies conducted in Olkiluoto, SW Finland, which target the rock volume planned to be used in geological disposal of nuclear waste. These investigations, conducted by POSIVA, currently provide an extensive dataset of fault-slip data (from tunnel, drill core and outcrop mapping), which have been further developed into a model over the brittle crustal evolution from 1.9 to 0.9 Ga by Mattila and Viola (2014). Their model is based on paleo-stress tensor analysis complemented with K/Ar determinations of the fault-infill minerals (Viola et al., 2011). The results show that there were 7 distinct stages of brittle deformation as presented in Fig. 1, where stages 4-7 represent the paleostress states during and after the emplacement of the 1.65-1.55 Ga rapakivi batholiths and are hence of particular relevance for this investigation.

Post-rapakivi deformation structures have been studied using the structural data from greisen-type veins, Satakunta sandstones, rapakivi granites and 1.27 Ga diabase dykes from the Olkiluoto area (Mattila and Viola 2014). Stage 4, as the first post-rapakivi stage, is represented as NE-SW oriented crustal extension, which corresponds to rifting that caused the deposition of the NW-SE elongated Satakunta sandstone formation. Furthermore, two major compressional stages 5 and 6 were observed in the modelling and from the patterns of diabase dykes: Stage 5 was represented by NNE-SSW -oriented compression after the emplacement of Rapakivi intrusions (Mattila and Viola 2014). The orientation of this compression rotated towards WNW-ESE by the late Mesoproterozoic Stage 6. The youngest of the recognized stages (Stage 7), reflects an E-W oriented tensional stress field, which likely occurred synchronous with the Sweconorwegian orogenic activity (Mattila and Viola 2014).

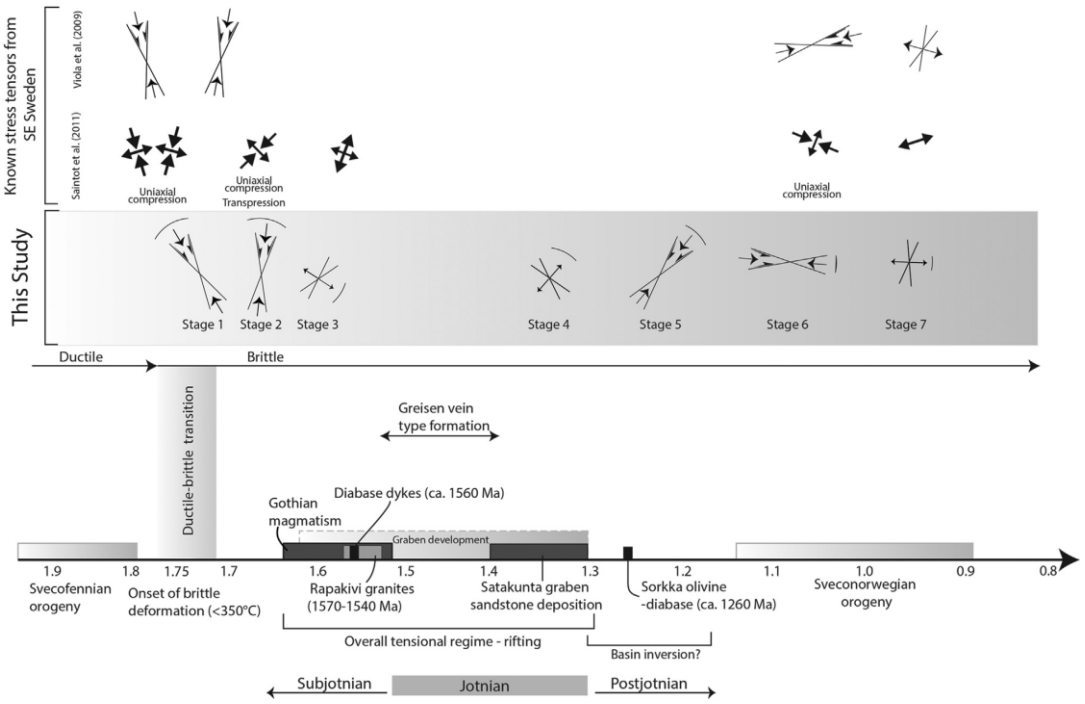

Fig. 1. Illustration presenting the model of the evolution of brittle structures in southwestern Finland constructed by Mattila and Viola (2011). Stages 4-7 are relevant for this work.

2.2. Geology of the study area

The study area of this thesis is located on the Island of Orrengrund, Gulf of Finland (Fig. 2A), which is, characterized by the anorogenic and isotropic (Fig. 2B) 1.6 Ga Rapakivi granite batholith (Vaasjoki et al. 1991; Rämö and Haapala, 1995). The recent study by Skyttä et al. (2021) within the area has given new insights towards the understanding how discrete faulting and kinematically linked damage zones form in homogenous crystalline rock, and how the faults and associated early-stage brittle fractures control the formation of later-forming regional fractures. The results and data in Skyttä et al. (2021) will be used as background for this investigation. In this work I will further develop the analysis into higher level of detail and correlate the results with the earlier findings.

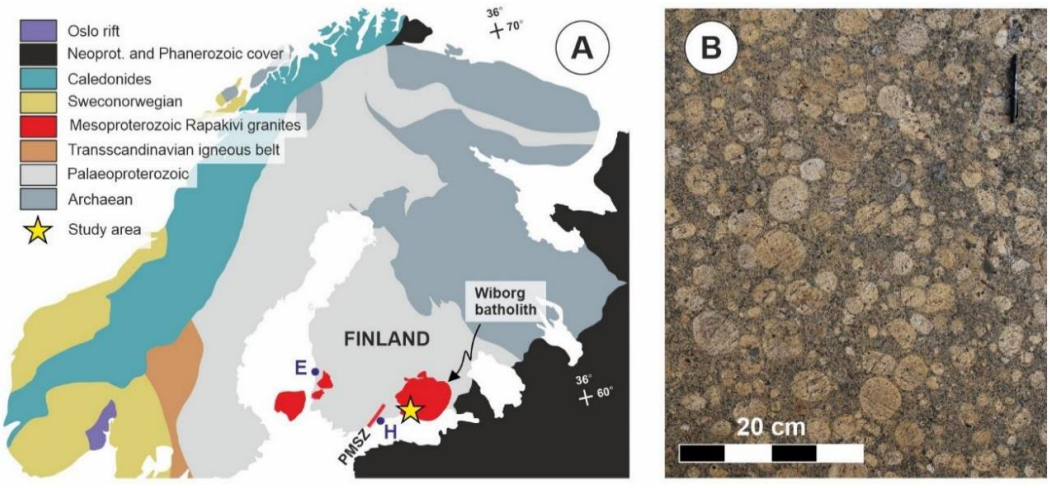

Fig. 2. A: Location of study area within the Fennoscandian shield (Skyttä et al. 2021). H = Helsinki. PMSZ = Porkka-Mäntsälä Shear Zone. B: Example picture from study site of homogenous undeformed Wiborg Rapakivi granite.

Figure 3 presents the rough overview of the study area of Skyttä et al. (2021) with fracture trace data used, and the study area of this thesis is highlighted with a red dashed line (Fig. 3; A), and the location of the studied sinistral fault with a purple circle (Fig. 3; B).

The area was divided by Skyttä et al. (2021) into seven structural domains acknowledging the spatial variation of fracture patterns as characterized by the variation of fracture intensities, orientations, scalability, and connectivity. The interpretations revealed N-S trending sub-vertical early-stage faults linked with synchronous kinematically linked NW-SE and NE-SW trending fracture sets. The N-S trending faults have well-developed damage zones with the recognized wall, tip, bend, and linking damage patterns, which have preserved the structures associated with the early stages of faulting. Moreover, the overprinting regional or background fracturing indicate that the faults were reactivated as they show fracture patterns deviating from the orthogonal regional patterns.

Skyttä et al. (2021) describe the evolution in two phases of which the first phase covers the "generation of normal damage zones within the immediate vicinity of the faults" and the formation of wide damage zones in between parallel but separated segments of N-S trending faults. The second phase, in turn, represents the generation of the regional fractures, which was associated with reactivation of the damage zone within faults identified from deviations of orientation and intensity of fracturing associated with faults and fault intersections. As a result, specific fault-bound fracture domains were generated.

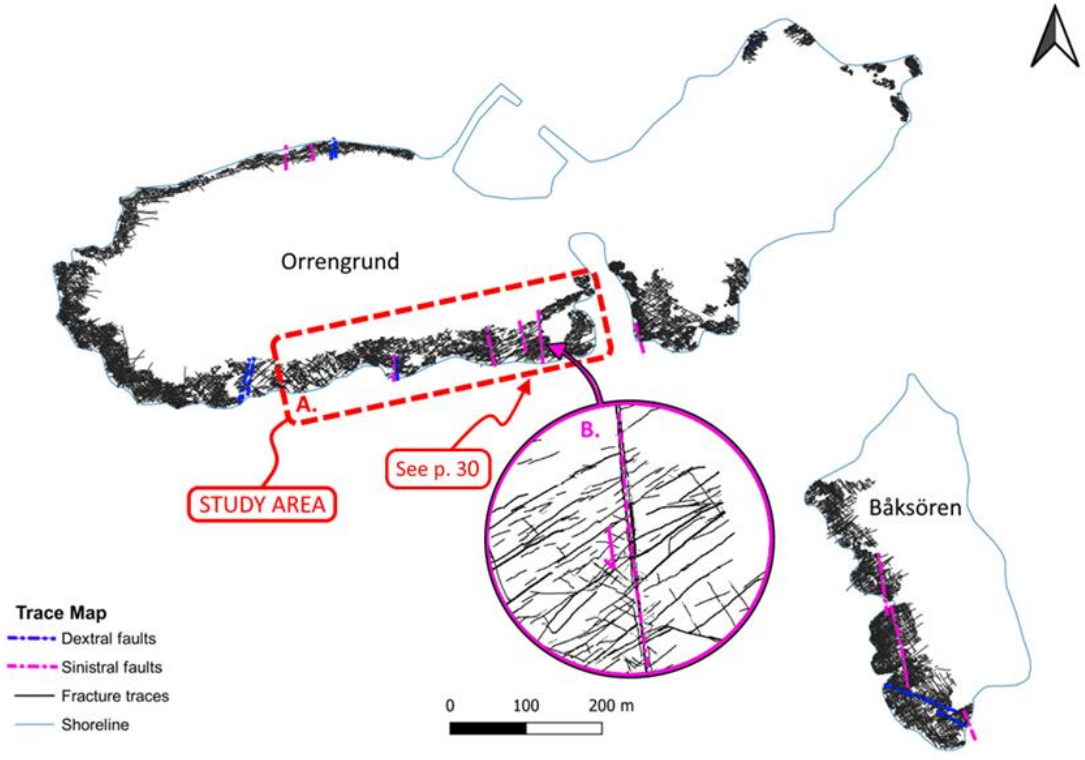

Fig. 3. Extent of study area (A) and location of studied sinistral fault (B) shown on trace map over all UAV-scale fracture and fault trace data of the Orrengrund island. Modified after Skyttä et al. (2021).

3. Macro- and micro-scale brittle deformation structures in crystalline rock

3.1. Macro-scale brittle structures

3.1.1. Fractures

The term fracture is used for a variety of structures, including veins, dykes, joints, deformation bands and faults (Peacock et al. 2016). Fractures are planar or sub-planar discontinuities which compose of two parallel surfaces that coalesce at the fracture front. Fractures are typically classified into sets, and these sets and individual fractures define fracture networks, where individual fractures intersect at intersection points or intersection lines (Sanderson and Nixon, 2015; Peacock et al. 2018). The properties of the fracture network may be characterized by the geometrical arrangement of the fractures, such as location, length, orientation, density and aperture, and the connectivity between the fracture (Berkowitz 2002). In its simplest form the fracture network may consist solely of just one fracture set, but more typically the fracture network comprise several sets, with diverse orientations, fracture types and properties, which all contribute to the properties of the rock volume being investigated (Manda and Horsman 2015; Peacock et al. 2016; Peacock et al. 2018). A fracture network may be a result of one single deformation event, in which case all the fractures are likely kinematically linked. However, the networks typically comprise fractures and fracture sets associated with separate geological events characterized by variable conditions, and the older members of the fracture network may have been reactivated during the overprinting events (Peacock et al. 2018). Based on the above, adequate characterization of the fractured volume of crystalline bedrock requires that both the individual fractures, as well as the fracture network must be analyzed.

3.1.2. Subsidiary fracturing

Secondary fractures associated with shear deformation within the brittle deformation regime have been studied e.g. by Cloos (1928) and Riedel (1929), who defined the Riedel shear structures as Riedel shears (R) and conjugate Riedel shears (R'; Hills, 1963; Tchalenko, 1970). The Riedel shears (R) are the earliest subsidiary structures which generate when faulting starts, and they typically propagate out of the parent fault (Tchalenko 1970). R-shears show acute angles 10-20° to the hosting faults, and the structural facing with the hosting fault is dependable on the sense of displacement along the main fault: dextral and sinistral faults are associated with clockwise and anticlockwise trending R-shear orientation with respect to the main faults trend, respectively). The R shears occur commonly as en échelon arrays, which are synthetic to the sense of movement across the main fault, and, for this reason, are useful for interpreting the kinematics of the faults and deformation zones (Tchalenko 1970). The variation of the distribution, strike, dip, and length of the early Riedel shears may be associated with variability in conditions such as the initial stress state, the complexity of the basement fault configuration (Tchalenko 1970). The other common type of Riedel structures, the R' shear fractures are antithetic with respect to the hosting fault. They form simultaneously or

after the R shears and characteristically display angles (75-90°) to the main fault (Tchalenko and Ambraseys 1970). Due to their later generation, the R' shears tend to generate within the overstepping areas of overlapping R shears. With progressive development of the Riedel system, P-shears are formed, given that the fault displacement is larger than that required for the generation of the R and R' shears (Tchalenko 1970; Naylor et al. 1986; Sylvester, 1988). Similar to the R shears, the P shears may occur as en echelon arrays, and their angle with the fault plane is typically small, but the geometric relationship (or asymmetry) is opposite to the R shears (Tchalenko 1970). Further, P shears are contractional in character, and thus accommodate fault parallel shortening as deformation propagates. Theoretically speaking, there is a possibility for the presence of P' shears, which are conjugate to the P shears, but such P' shears are difficult to be distinguished from the orientationwise very similar R' shears. One more feature within the Riedel system of structures are the T-fractures (= extension fractures) which are synchronous with the R shears and share the same geometric relationship with the main fault, but occur at larger, approximately 45-degree angle to the main fault (Tchalenko and Ambraseys 1970). Moreover, Y shears are microfractures, which are synthetic with the main fault, and occur sub-parallel to the main fault. Within narrow faults with roughly planar geometries, all Y shears may define an anastomosing network of fault-associated fractures (Woodcock and Schubert 1994).

3.1.3. Wing-cracks and horsetail fractures

Wing-cracks form as tensile mode I fractures at a relatively high angle to the slip surface (Brace and Bombolakis 1963; Lajtai 1971). Wing-cracks form in uniaxial compressive conditions, either within conditions of high pore pressures or under low effective stresses (McGrath and Davison, 1995). As the wing-cracks are mode I (or opening mode) structures, they are commonly associated with mineral fillings, which are indicative of fluid flow within the subsurface fracture networks (Mutlu and Pollard 2008). Wing-cracks initiate at the tips of pre-existing structures such as shear fractures or faults, i.e. they do not propagate along their own plane (Brace et al. 1966; Cruikshank et al., 1991; Bobet 2000). Wing-cracks may be found either at one or both terminations of the parent structure. Experimental investigations and numerical analyses indicate that wing-cracks tend to propagate from the tip of the flaw and curve towards parallelism with the orientation of the main principal component ($\sigma 1$) of compressive stress (Brace and Bombolakis 1963; Lajtai 1971; Horii and Nemat-Nasser, 1986; Petit and Barquins 1988). Extending the lenght of the wing-crack requires that the magnitude of the compressive stress is increased (Bobet 2000), but further experiments conducted within 3D-environment show that the growth of wing-cracks have certain limits, and the size of the wing-crack may not exceed the size of the initial discontinuity along which it initiated (Dyskin et al. 1999).

Other structures geometrically and mechanically comparable to the wing-crack are called horsetail and/or pinnate fractures (Granier 1985; Petit and Barquins 1988). These structures are typically less distinct, and their angle to the hosting structure is characteristically smaller than for the wing-cracks with respect to the parent structure, (Granier 1985; Hancock 1985; Petit and Barquins 1988; Engelder 1989; Kim et al. 2004). Horsetail structures generate in biaxial conditions and occur within the localized zones of extension along faults, resulting as e.g. curvature of the fault (Granier 1985; Petit and Barquins 1988). In comparison with wing-cracks, horsetail fractures display gradual fading-out towards the tip of the fault (Kim et al., 2000), and the horsetail structures may experience reactivation as synthetic faults during overprinting tectonic events (Granier 1985; Kim et al. 2001a). Moreover, horsetail fractures display symmetrical arrangements around the initial flaw, whereas the wing-cracks occur only on one side of the hosting structure (Brace and Bombolakis 1963; Fossen 2010).

3.2. Damage zones

Brittle faults comprise of central cores or core domains, which accommodate (the most of) the displacement along the fault. The core is surrounded by fault damage zone (DZ), which is overall less intensely deformed (Billi et al. 2003; Peacock et al. 2017), but still more deformed than the surrounding rock unaffected by faulting. The intensity of DZ fracturing is shown by increased fracture intensity and contrasting fracture orientation distributions (Chester and Logan 1986; Ishii 2016). Damage zones are kinematically associated with the fault, and hence generated as response to fault propagation, interaction, and build-up of slip along the fault (Cowie and Scholz 1992; McGrath and Davison 1995; Caine et al. 1996; Kim et al. 2004; Childs et al. 2009; Choi et al. 2016; Peacock et al. 2017). Secondary fracturing within the DZs is typically distinguishable (Martel et al. 1998) and the variety of geometries and fracture patterns can be linked to different DZ types (Kim et al. 2004), which generate as response to variations in the local stress field orientations ranging from variations in the fault geometry and interaction with other faults (Chester and Chester 2000; Faulkner et al. 2011). Additionally, fault initiation style provides the ultimate control over the fault-rock characteristics (Crider and Peacock 2003), with contributions from variations in lithology, rheology, attitude and type of foliation or bedding relative to the e.g. fault type, fault slip orientation, and the ambient stress state (Kim et al. 2004).

Earlier DZs classifications have focussed on the spatial occurrence of the DZ with respect to the fault (tip, wall, and linking DZs; Kim et al. 2004), whereas recent updates additionally address the interaction between different components of the fault system (Choi et al., 2016; Peacock et al., 2017). According to Kim et al. (2004), tip-DZ is spatially associated with the tip of the fault, and display versatile structures: wing-cracks, horsetail structures, syn- or antithetic faults, splays or branches are commonly found particularly along the terminations of strike-slip faults (Kim et al., 2004; Peacock et al., 2017). Synthetic faults comprise fault

splays or branches, which share the sense of movements with the master fault. By contrast, the antithetic faults show opposite movement senses, and increased lengths and spacings away from the fault tip (Kim and Sanderson, 2006). Wall-DZ is associated with the propagation of faults, is located along the fault (both sides or one side) and occur typically as extension fractures or en echelon swarms of fractures (Kim et al., 2004). Wall DZ may be continuous with the tip-DZs in which case the combined wall-tip-DZ may extend along the full length of the fault trace. Parallel, but overlapping fault segments are brought into dynamic interaction through development of linking DZ, which occurs at the overstepping area of the geometrically isolated fault segments. The character of the developing fractures depends on whether the step-over is contractional or extensional in character (Fig. 4; Kim et al., 2004).

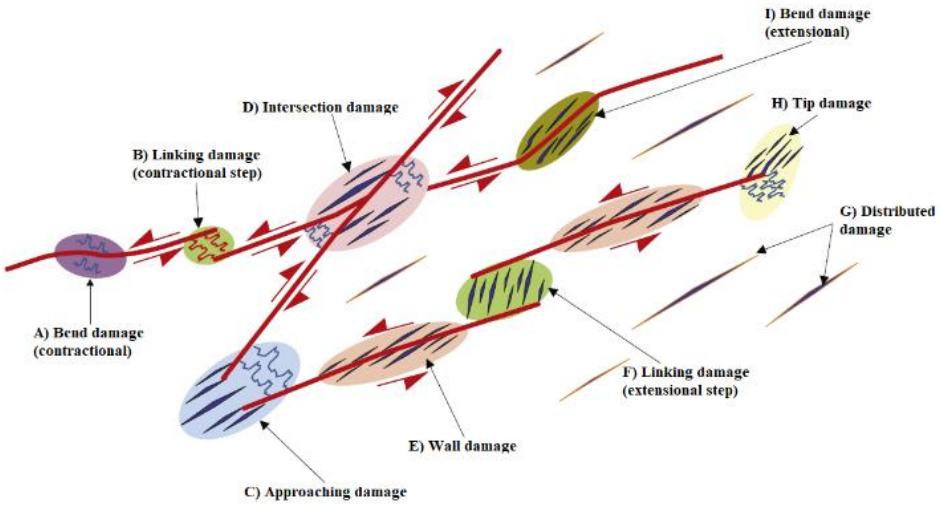

Fig 4. Damage zone types as described by Kim et al. (2004) and Peacock et al. (2017). From Peacock et al. 2017.

The revised DZ-model of Peacock et al. (2017) addresses the uncertainties and challenges in determining the DZ type by incorporating constraints about fault interaction, irrespective of relative orientation or age (Peacock et al., 2017), which is further sub-divide into classes fault *intersection*, *fault bend*, and *approaching* DZ.

Intersection DZ, for example, may comprise abutting or cross-cutting faults, even though they were not synchronously generated, and hence not kinematically linked (Peacock et al., 2017). By contrast, approaching DZs are associated with faults that do not physically intersect each another, but are still kinematically linked, which also means that displacement along one affects the other (Peacock et al., 2017). Fault bend DZs develop in releasing or contractional fault bends along faults, as response to resolving of the regional stress into local domains of extension or compression (Kurt et al. 2013; Janecke et al. 2013). Peacock et al. (2017) further define a term distributed DZ to indicate how the precursory fault damage is distributed within an area characterized by intensity above the surrounding areas.

The revised usage of the DZs provides tools to address post-fault deformation, mineralization, and stress development (Peacock et al. 2017), but may also lead to additional uncertainties particularly when exposures are limited (Rotevatn and Fossen 2011; Peacock et al. 2017). DZs are significant for many geological applications as they define pathways for fluid flow in crystalline crust (Caine et al. 1996), and hence contribute to understanding of the ore-deposit modelling (Brogi 2011), hydrocarbon reservoirs (Aydin 2000), and groundwater (Lopez and Smith 1995; Cox 1999; Dimmen et al. 2017). Further assessment of DZs, together with fault initiation and propagation, can be used to understand regional strain patterns and earthquake rupturing (Scholz and Cowie 1990; Crider and Peacock 2003; Kim and Sanderson 2008).

3.3. Microfractures

3.3.1. Morphological classification

Faults hosted by crystalline rocks initiate and grow through interaction of microscopic discontinuities (Crider 2015), which represent pre-existing networks of microfractures, as well as cleavage planes of (typically anisotropic) minerals. For the purposes of understanding the inherently variable and complex arrangements of microfractures, (Kranz 1983) has sub-divide them into four morphological categories: coincident grain boundary cracks, non-coincident grain boundary cracks, intracrystalline cracks, and cleavage cracks.

The occurrence of grain boundary cracks is limited to individual mineral grains: coincident grain boundary cracks are elongated along the space between the individual grain and the surrounding matrix, whereas cracks propagating into the grain from the surrounding matrix are called non-coincident grain boundary cracks (Krantz, 1983).

Intracrystalline or transgranular cracks (Kranz 1983) are connected through several grains and occur predominantly in rocks that experienced thermal or mechanical stresses, and this results in their characteristically sharp walls and tips. Intracrystalline cracks generate as mode I fractures, in association with extension caused by minor slip events along the hosting displacement planes (faults; Krantz 1983), and these fractures may be non-planar in 3D. The lengths of these fractures are typically smaller than the grain size of the rock, and they have a very limited aperture. The cleavage cracks represent fractures occurring along the cleavage planes of minerals grains, and consequently, their orientation is largely controlled by the crystallographic properties of the hosting mineral species (Kranz 1983).

3.3.2. Generation mechanism of microfractures

Interaction between microfractures is essential in determining how faults are initiated (Crider 2015). For this reason, understanding the governing physical processes is important. An attempt towards this has been given by Kranz (1983), which, based on both natural and experimental studies, provides seven different mechanisms responsible for the generation of microfractures (Table 1).

Table 1. Generation mechanisms of microfractures and their descriptions according to Kranz (1983).

Mechanism	Description
Twin lamellae cracking on grain boundaries	E.g. crack nucleation in calcite twin lamellae.
Strain energy relaxation of deformation lamellae	Kink band boundaries and discontinuity arrays cause compressional or extensional strains. This strain can be relieved thus causing the nucleation of micro-crack.
Cleavage separation	E.g. cracking in biotite through the plane of lowest atomic bond strength.
The concentration of stress in neighboring grain boundaries and cracks	Changes in stress field due to cavities in the rock.
Rotation and translation of grains	Deviatoric stresses can lead to grain boundary sliding, thus causing rotations of grains. This can happen e.g. in cataclastic deformation in active faults.
Elastic compliance contrast in neighboring grains and matrix	Boundary tractions generate under stress due to different mechanical properties in interlocked mineral grains.
Thermally-induced micro-cracking	Differential thermal expansion of rock mass leading to generation of tensile stresses. This mechanism plays the dominant role in crack initiation mechanisms in granite due to the differing thermoelastic modulus of quartz and K-feldspar.

The dependence between the rock (micro)fabric and fracture generation is shown in Fig. 5, which illustrates uniaxially loaded rock samples on a mesoscopically isotropic granite, foliated gneiss, and a granite with a pre-existing weakness (Figs. 5a-c, respectively; Crider, 2015). In the isotropic granite, micro-faults developed through propagation of stress-parallel fractures, which lead to formation of rock columns, that eventually fail and slide. In contrast, slip surfaces into the foliated gneiss are developed through interaction of grain boundary cracks and connection with intracrystalline crack, in a process significantly affected by the rock anisotropy. In the third example, an initial process zone is developed by Mode I fractures, which further develop into a fault as a response to propagation of Mode III shear fracture tip, defining the propagation of the fault through the rock.

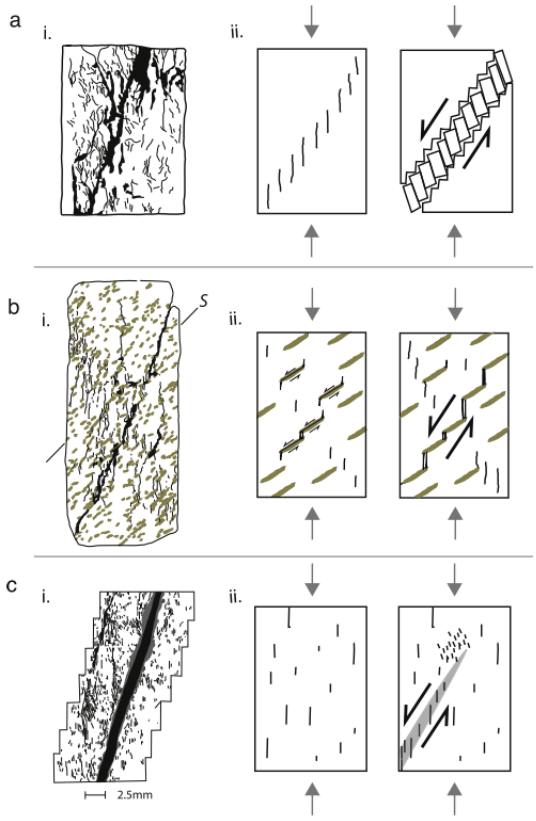

Fig 5. Illustrative picture of Chelmsford granite (a), Four-mile gneiss (b), and Westerly granite (c) presenting the sketched fracture patterns after uniaxial compression of rock sample (i). In addition, conceptual models of fault initiation (iii) are shown with nucleation cracks (ii). According to presented models, fault can initiate through grain rotation (a; iii), grain boundary crack linkage (b; iii) or tail-crack development (c; iii). Fig. from Crider (2015).

4. Data and methods

4.1. Fracture trace data on UAV- and SLR orthophotography mosaics (Scales 1 and 2)

The scale 1 (UAV-scale) orthophotography data used in this thesis is portion of the data set used in Skyttä et al. (2021). The data used in this thesis covers approximately 400 m long shoreline with almost continuously well-exposed rock outcrops (Fig. 6A). In taking of orthophotos in Skyttä et al. (2021), the flight altitude of the drone was kept at 20 m which resulted in a 0,55 cm pixel size for the single raster image. The images were taken with 60-70% overlap, and 10 pcs of VRS-GPS ground control points were used for georeferencing the images into one ortho-mosaic by using Agisoft PhotoScan software. The orthophoto mosaic was after imported into ArcGIS software for fracture trace digitizing. The digitizing work of scale 1 (UAV) fracture network was done by Skyttä et al. (2021) whereas refined scale 2 (SLR-scale) data was digitized by me within this thesis.

In ArcGIS digitization, the interpretation boundary was created as a polygon vector feature, whereas for the fracture traces the single polylines were used (Fig. 6B). At least four rules according to Nyberg et al. (2018) had to be followed in digitization of fracture traces to avoid generation of topologically inconsistent fracture networks:

- A maximum of two fracture traces can intersect through the same node
- Fracture traces cannot intersect without snapping
- Fracture traces cannot form isolated loops
- Fracture traces cannot be digitized starting from tip of existing fracture trace

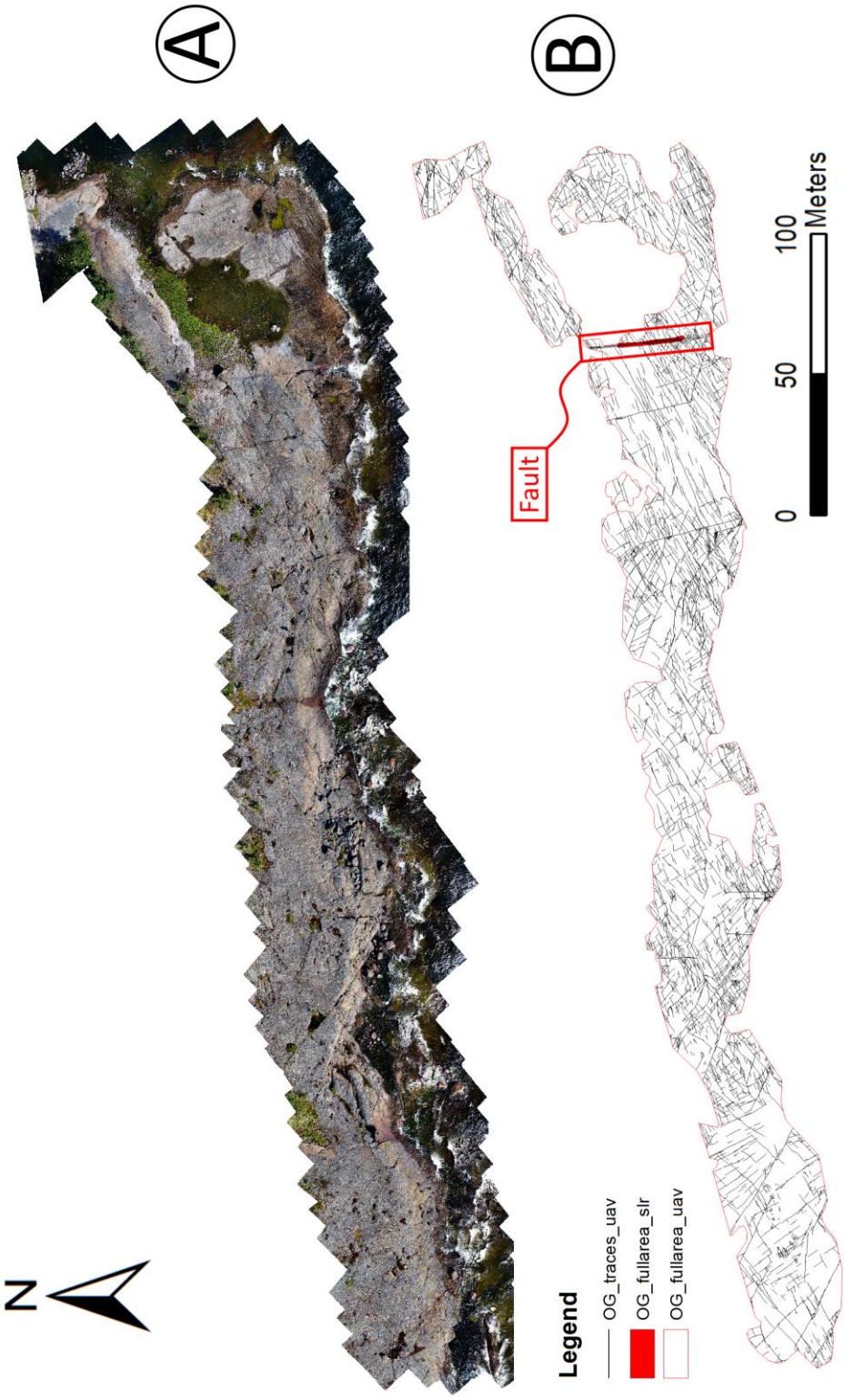

Fig. 6. A: UAV-orthophotography mosaic of the study area. B: Fracture trace data digitized on the UAV orthophotography mosaic. Location of the studied sinistral fault (Fig.7) is shown by the red box.

The second data set (Scale 2) consists of 1,5 m x 17 m SLR-imagery taken on the sinistral fault located in the eastern part of the study area (Fig. 7B). The photographs were taken with a high-resolution SLR camera mounted on tripod, resulting in a 0,029 cm pixel size which can capture structural features of rock in detail of an individual mineral grain. After compiling the SLR-scale ortho-mosaic from images, the raster image was georeferenced using the UAV-scale raster image. In this way, the geometrical features of the fracture networks of SLR- and UAV scales are comparable to each another on the same scale.

The fracture trace digitizing process for the SLR scale was identical to the UAV scale. Fig. 7B shows the SLR-scale ortho-mosaic with a digitized fracture network (Fig. 7A). In Figures 7C and D, the level of detail is highlighted with a centimeter scale close-up on raster imagery and trace datasets.

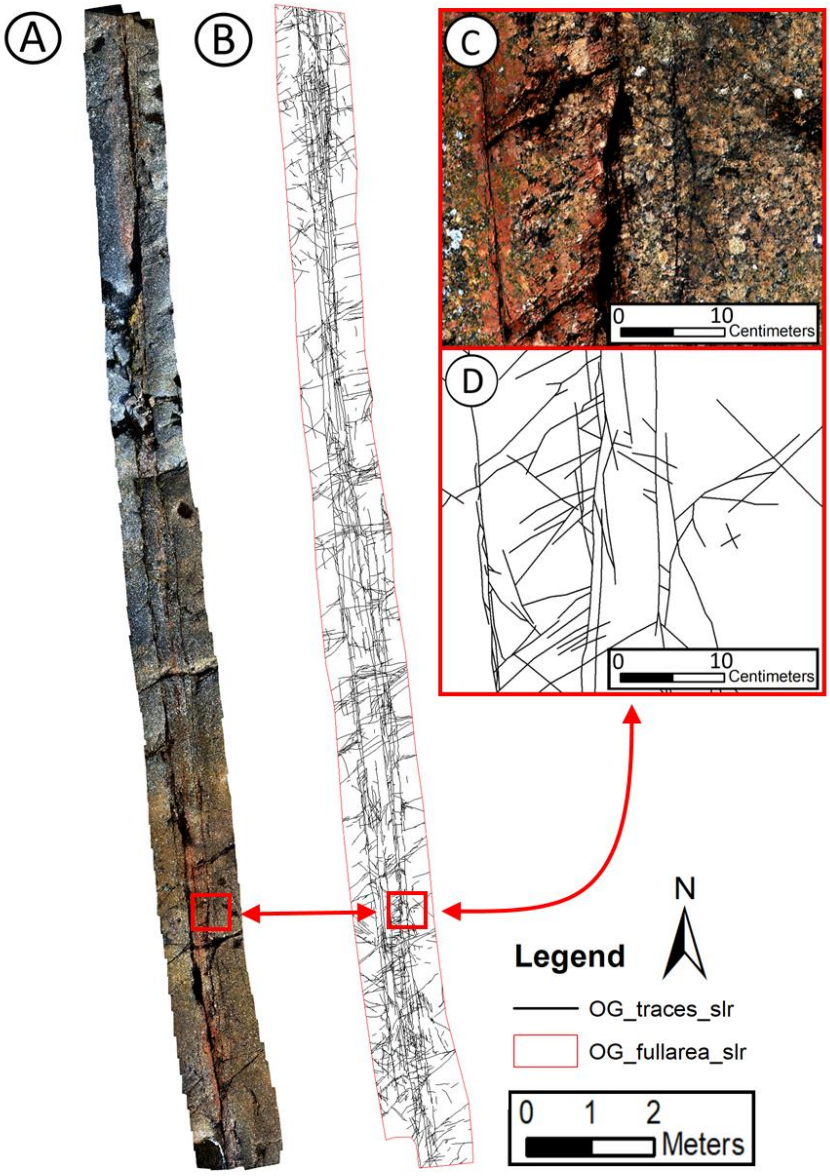

Fig. 7. A: SLR-camera-scale orthophotography mosaic of the study area. B: Fracture trace data digitized on the SLR orthophotography mosaic. C: Figure showing the centimeter-scale detail of SLR fracture trace dataset.

4.2. Fracture orientation field-measurements

In addition to ortho-photogrammetry data obtained in UAV and SLR scales, 24 geological compass joint measurements were included in the characterization of fracture orientations associated with the sinistral fault and syn-fault fractures (see location in Fig. 6B) studied in this thesis. These measurements were utilized to give a 3D reference for the 2D interpretation done on the fracture networks within the studied fault.

4.3. Oriented rock samples for grinding tomography (Scale 3)

A few oriented rock samples were collected from Orrengrund Island during mapping works in summer 2019. For this thesis, the sample ORR-1.3-2019 (Fig. 8B) was selected for the grinding tomography modelling. Fig. 8A shows the location of the sample within the visible part of the sinistral fault. If we take a closer look at the location in Fig. 8C, the sample represents the fault core of the sinistral fault, and the micro-structures within this fault core zone are the main interest of this thesis.

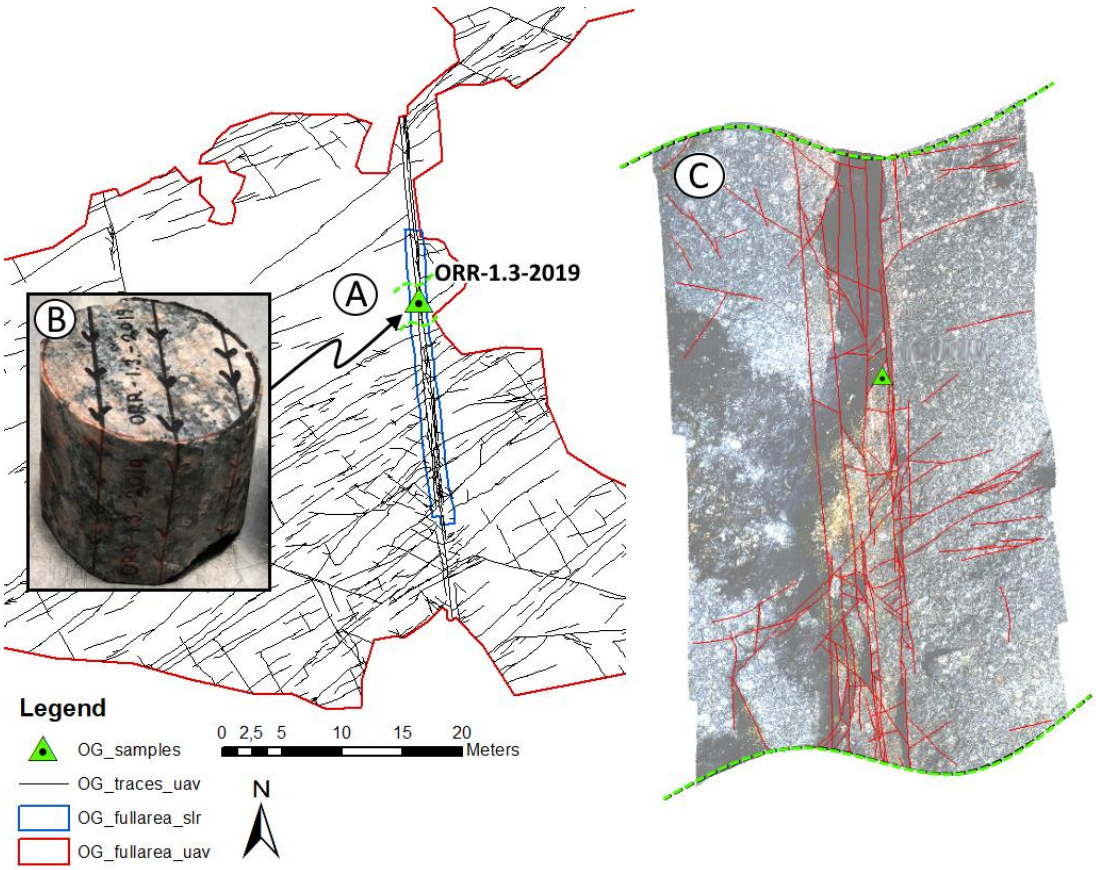

Fig. 8. A: Map showing the location of the sample ORR-1.3-2019. B: The location of sample within the SLR-scale fracture networks is presented in (C).

Before using the GRN16 for grinding tomography, test samples were first prepared in a laboratory using the following sample preparation procedure with three major steps shortly described below:

- **Step A (Fig. 9A):** Minimum 50 mm thick slice is cut off the hand specimen with a rock saw in the horizontal direction. Both bottom and top cut surfaces were perfectly parallel.
- **Step B (Fig. 9B):** 50 mm diameter circle and north arrow is drawn on the cylindrical sample. The circle is a reference for drilling the sample using a stationary rock drill located in the laboratory. After drilling the sample, the bottom and top surface of the sample are finished with the hand-operated Kugelmüller grinder machine if needed.
- **Step C (Fig. 9C):** Sample is glued on 52x52 mm glass sheet with two-component adhesive. Before using the adhesive, the North arrow is marked on the glass by using the North arrow in the rock sample as a reference.

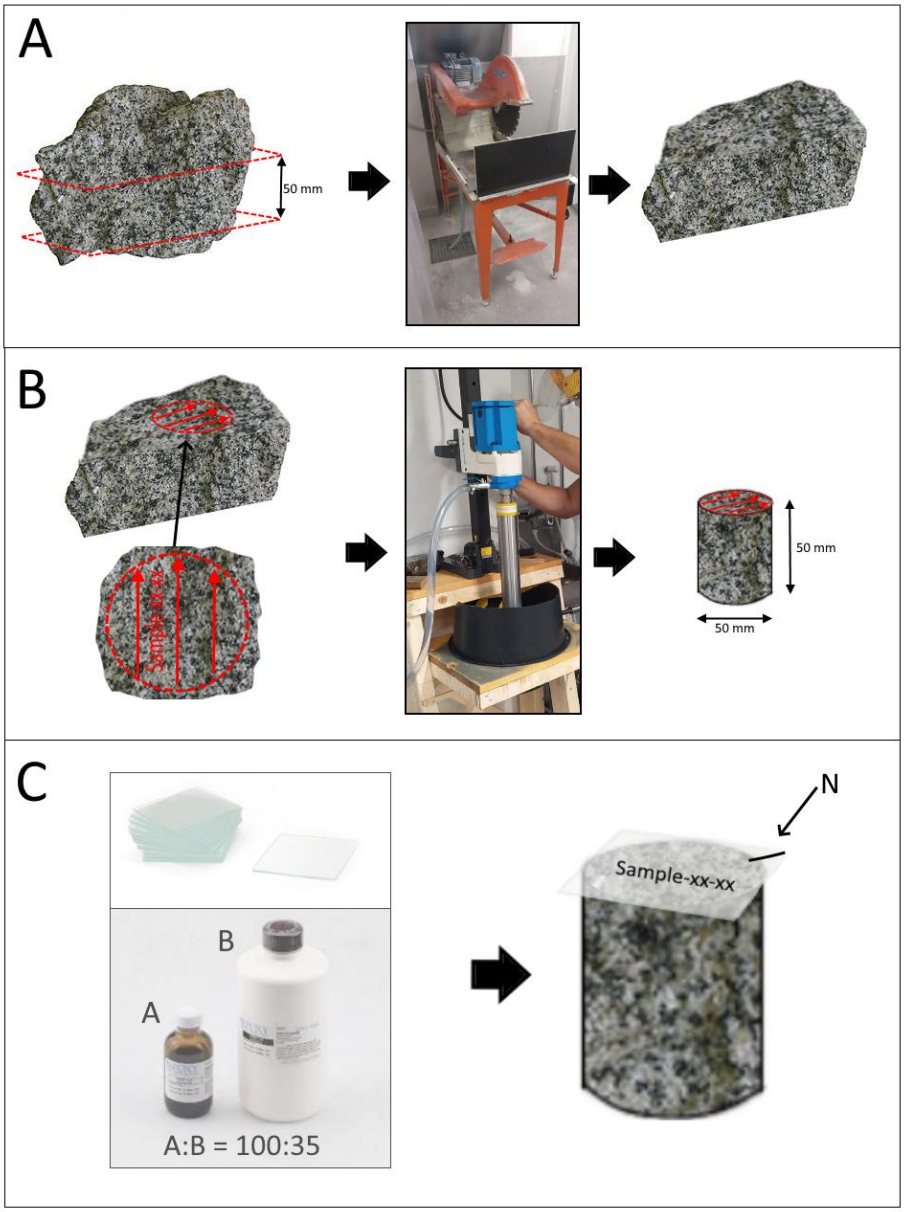

Fig. 9. Illustration of the steps in 3D tomography sample preparation procedure. Step A: sawing of the sample. Step B: Marking of the location, name, and North direction on sample e.g. in corner of the glass, depending in which orientation the sample is glued (in case of oriented samples). Step C: Gluing of the sample on glass using two component adhesive.

4.4. 2D-fracture trace network analysis

The 3D geometry of the fracture networks can be presented as finite surfaces, which terminate as tip lines. When a 3D fracture network intersects a 2D-surface, the individual fractures form a 2D fracture network, for which geometrical properties can be derived using a set of parameters such as i.e. size, orientation, and length. However, these parameters have exact dimension, which changes when the network is transformed with respect to e.g. strains or scale (Sanderson and Nixon 2015; Nyberg et al. 2018). For this reason, new approach addressing the dimensionless parameters have been developed such as topological analysis methods.

Topological analysis methods have been recently established for fracture network studies with the focus on the quantification of the dimensionless parameters in the fracture network (Sanderson and Nixon 2015). Derivation of fracture network connectivity parameters is done by defining the termination, abutting, or cross-cutting points of fracture with different types of nodes, where I-node represents terminating fracture, Y-node abutting fracture to another fracture, and X-node cross-cutting of two individual fractures (Fig. 10; Sanderson and Nixon 2015). As we are dealing with a network of fractures, the nodes subdivide the network into branches, which are defined by the type of nodes on each end of the branch (I-I, C-I, and C-C). The analyzed fracture network is always limited by interpretation boundary. The traces that intersect this boundary form nodes called E- and U-nodes (Nyberg et al. 2018). The E-node is the intersection point of the trace and interpretation boundary whereas the tip of trace left outside the interpretation boundary is called U-node.

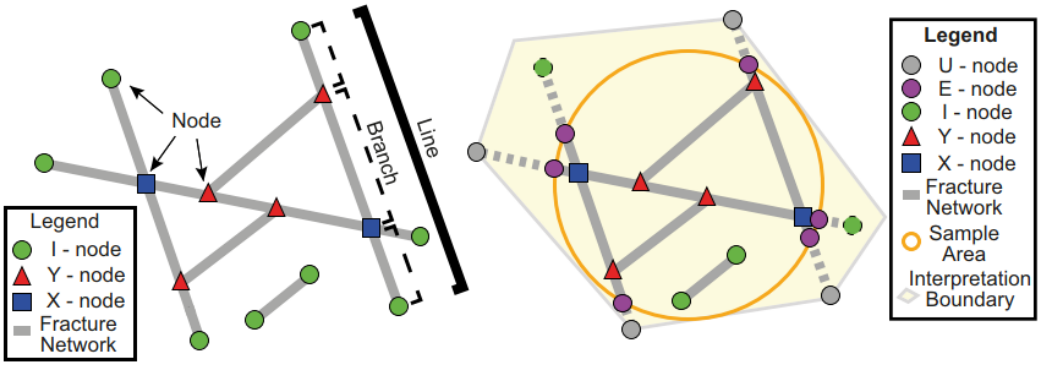

Fig. 10. Left: Sub-division of fracture traces forming the network into nodes and branches. Right: Use of interpretation boundary. Figure modified after Nyberg et al. (2018).

Node and branch counting are important tools to evaluate the topology of the fracture network (Sanderson and Nixon 2015). As an example, the Figure 11 presents a triangular plot with I, Y, and X node proportions, where three natural fracture networks and two stochastic trace line simulations are plotted (Sanderson and Nixon 2015). As seen from the Figure 11, the abundance of I-nodes increases the amount of isolated fracture tips. The Y-nodes, in turn, decrease the amount of isolated fracture tips by terminating the fractures as abutments, which plays an important role in the connectivity of natural fracture networks (Manzocchi 2002). The

continuation of fractures is achieved with X-nodes by intersecting other fractures. Figure 11 illustrates (yellow boxes) how the proportions of different nodes affect the different fracture networks.

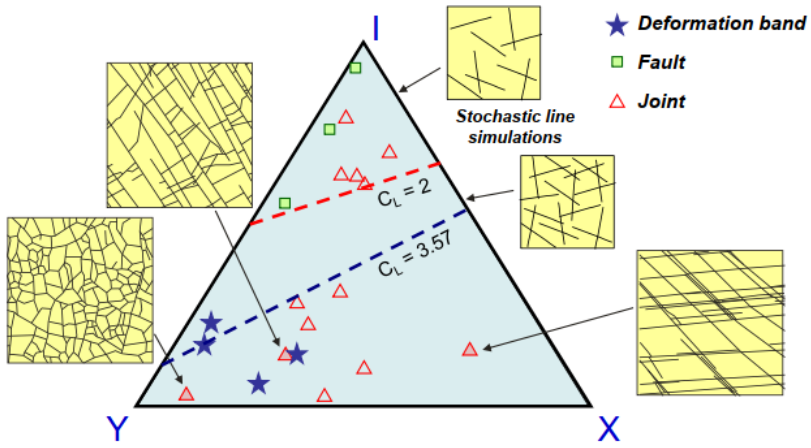

Fig. 11. Triangular node plot used to illustrate the proportions of I, Y and X nodes. Examples of natural fracture networks and stochastic computer line simulation results are plotted as an example. Figure from Sanderson and Nixon (2015).

In this thesis, the fracture network topology analysis is conducted as a 2-dimensional background study for linking the modeled 3D fracture networks into the regional framework. The analysis was done using Python-language-based Fractopo software developed by Ph.D. student Nikolas Ovaskainen from the University of Turku (Ovaskainen 2021; Fig. 12). The software uses fracture traces and interpretation polygon in vector form as input data, which will be validated or fixed by the program (correcting the possible errors in the network which will affect the analysis). The validated data will be divided into nodes and branches. The software executes analysis on selected interpretation boundary, and outputs rose plots for orientations, length distributions of branches and traces, and topological parameters such as node and branch proportions, as an example.

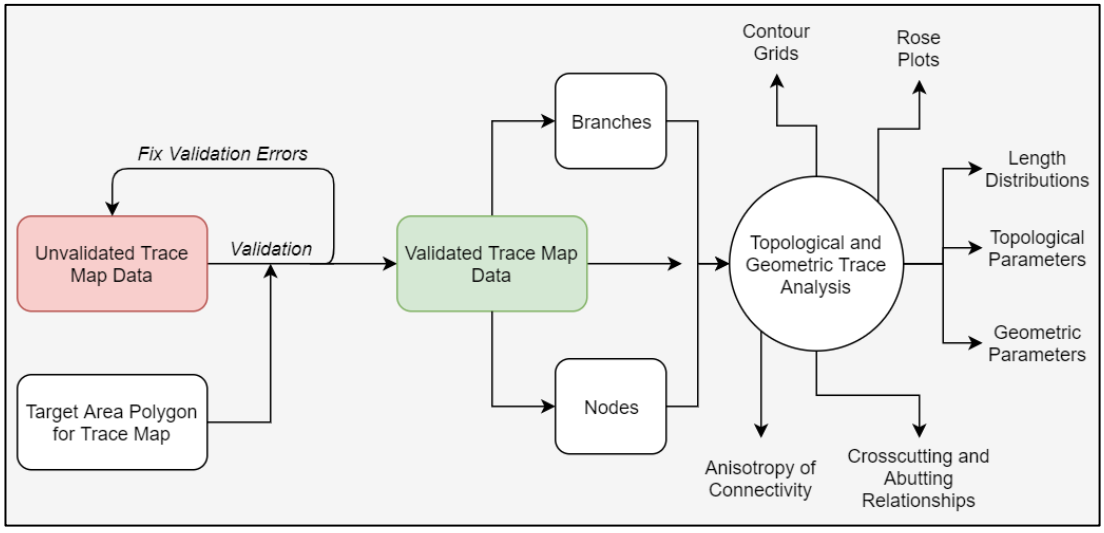

Fig. 12. Overview of the analysis procedure using Fractopo software (Ovaskainen 2021).

4.5. Automated 3D-grinding tomography

4.5.1. Application of tomography methods in geosciences

In 3D-modelling, tomography methods provide the means to view into the sample through successive 2D-sections, which eventually allow defining the dimensions and volumes of desired objects (Pascual-Cebrian et al. 2013). In the field of geosciences, grinding tomography has been applied to the study of fossils, and x-ray microtomography (or CT-scanning) to image fracture propagation in rocks (Pascual-Cebrian et al. 2013; Nasseri et al. 2011).

There are two alternative methods (Fig. 13): In the preservative method, the sample is studied utilizing e.g., X-ray (CT = computed tomography, XMT = X-ray micro tomography, or SRXMT = synchrotron radiation X-ray microscope), neutron-tomography, or MRI (= magnetic resonance imaging) technology. In contrast, the non-preservative methods involve either grinding or cutting the sample to expose new surface to be taken with high-resolution cameras or scanners, and hence lead to destruction of the sample.,

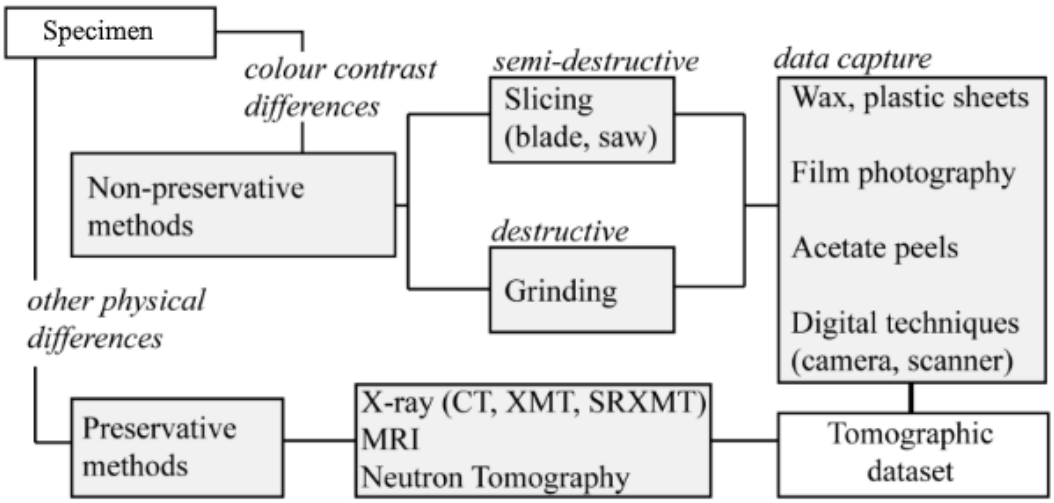

Fig. 13. Graph showing the division of non-preservative and preservative tomography methods used in geosciences. Modified after Pascual-Cebrian et al. (2013).

X-ray instruments are often used as non-destructive tomography instrumentation (Pascual-Cebrian et al. 2013). X-ray tomography is one of the most common non-destructive method. It utilizes the attenuation coefficient of the material, which is dependent on the density of the material. Consequently, individual mineral species within polymineral rock sample can be segmented, taken that the density contrasts with the neighboring minerals are large enough, and further displayed as 3D-voxel map. (Pascual-Cebrian et al. 2013). However, if no adequate density contrasts are present in the sample, the non-preservative methods may provide an advantage of recognizing features with similar densities but contrasting visual appearances. An example would be fractures filled with a material with the same density as the surrounding material. This is one of the topics discussed within this thesis.

4.5.2. Collection of grinding tomography data with 3D-grinder

According to Pascual-Cebrian et al. (2013), grinding tomography methods have encountered major disadvantages in previous studies. These problems are factors such as:

- Low resolution in inter-section space
- Poor grinding precision
- Problems having a constant lightning condition on sample
- Missing of a method for alignment of pictures automatically (manual alignment is a slow and unprecise method)

In this thesis, we bring the grinding tomography method to a whole new level by compiling high-resolution 3D-microtomography models representing the 3D-networks of fractures within rocks samples. The tomography images are taken with the GRN16 grinding machine at the Geology Section, University of Turku.

GRN16 is a grinding machine initially developed for the automatized grinding of thin section samples. The machine has been operating since 2016, and successivcely further developed in collaboration with Astera Solutions Ltd, Apex automation Ltd, and Winkoms Open Microscopy Ltd. The development work involved add-on equipment and new software tools, and the outcome is a new functionality of automated 3D-grinding.

GRN16 grinding machine itself is a relatively complex piece of machinery consisting of hundreds of mechanical and electronic components, although the main components needed for the grinding tomography can be presented and explained as follows: One of the most important parts of the machine is the grinding chamber with the rotating specimen table (Fig. 14; component 1). This table has multiple vacuum holes and can be equipped with a separate stainless steel sample holder which can fit up to four 52*52 mm glasses, on which the up to 50 mm high cylindrical rock specimens are glued. Above the sample table is a spindle that rotates a diamond grinding wheel (Fig. 14; component 2). The speed and vertical position of the grinding wheel is controlled by a computer-controlled servomotor, the operation of which is mainly automated. The grinding is lubricated by an adjustable water syringe (Fig. 14; component 3). The lubricating water leaking into the vacuum system is led into the water separation tank thus can be emptied during the grinding activity without losing the vacuum (Fig. 14; component 5). The machine is controlled mainly by the control panel in the front of the machine (Fig. 14; component 7) and the grinding-related parameters, such as grinding torque may be monitored from the display above the machine (Fig. 14; component 8). To produce tomography data, the machine is equipped with a computer-controlled camera system, light sources for both UV and visible light (Fig. 14; component 4), and a ventilation system keeps the droplets and humidity away from the lens of the camera (Fig. 14; component 6). The

camera system is controlled by a PC with software designed for the purpose (Fig. 14; component 9).

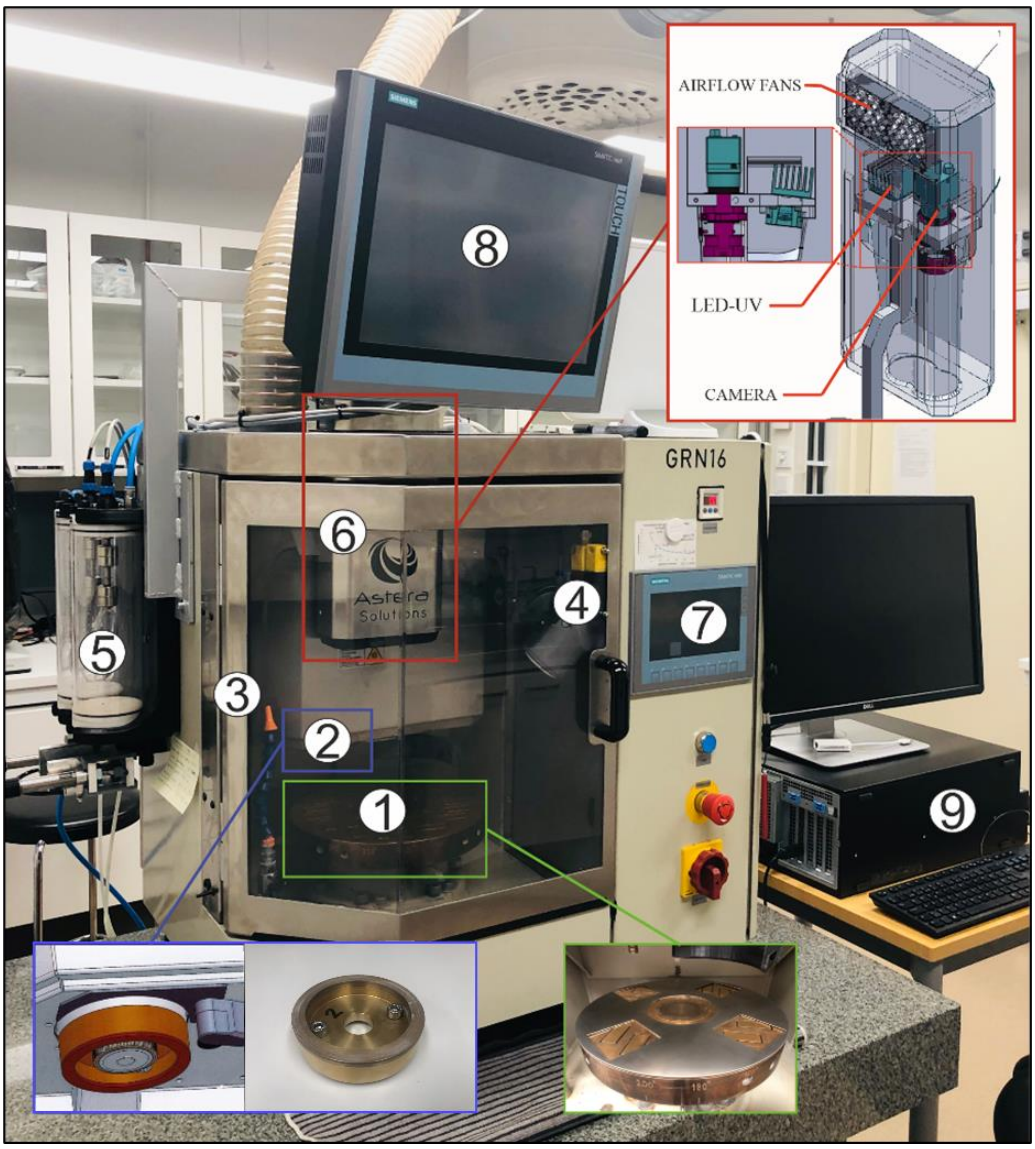

Fig. 14. The main components of the GRN16 –grinding machine: 1 = rotating sample plate with vacuum system providing the capacity for sixteen thin section samples and four 3D-samples (see the steel holder for 3D-samples), 2 = spindle with convertible diamond-coated cup grinding wheel, 3 = water lubrication syringe, 4 = lamp emitting visible light, 5 = vacuum water separation chambers (deviating from the picture, there is nowadays only one chamber at the back of the machine), 6 = camera system with servo motor (moving the camera in Z-axis), UV¬-A-led –light (365-405 nm wavelength), and airflow fans for preventing the dust and humidity to enter the camera casing and the lens (the design drawing is a rear view), 7 = Siemens KTP700 –main control panel, 8 = Siemens TP1500- display for monitor the position, vibration, and torque of the spindle, 9 = PC-unit controlling the camera system with Python-language based 3DUTUSGG- software when operating GRN16 in 3D-grinder mode.

When grinding the 3D tomography samples, the machine grinding cycle works as follows: the sample table rotates, the vacuum and steel rim hold the samples in place, and the machine grinds off a desired thickness of the sample (Fig. 15; part 1) with a water-lubricated (Fig. 15; part 3) diamond wheel. The grinding continues until the desired thickness is ground off the sample (Fig. 15; part 2). After grinding the slice, pressurized air is used to dry the sample surface from water droplets (Fig. 15; part 4). After this, the machine takes a digital image of

the upper surface of the sample, first in visible light and then in UV light (Fig. 15; parts 5,6 and 7). The purpose of UV light in the camera system is to recognize the pore spaces or open fracture systems from samples impregnated with fluorescence epoxy and compare algorithmically the images taken in UV- and normal light. However, this thesis is not covering such analysis as the studied Rapakivi rock samples do not have significant fracture apertures. The machine continues this cycle by taking successive images from the samples. As the grinding progresses, the camera keeps a constant distance to the top of the sample, and the Z-coordinate of the sample top is registered into the image file acquired by the camera. The images are automatically aligned by algorithms using a Python-based computer program. By combining these aligned images as an image sequence, a 3D tomography model can be constructed.

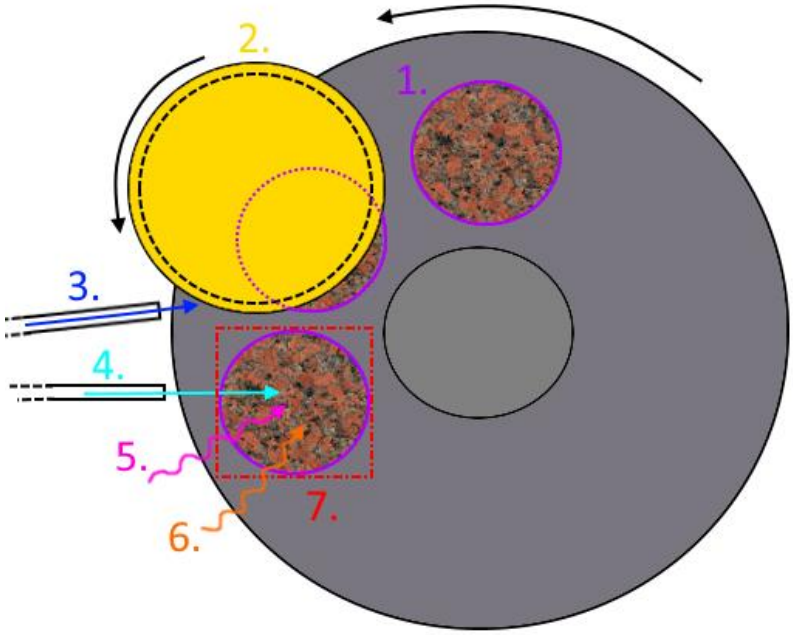

Fig. 15. Illustration of the grinding tomography procedure cycle: 1 = rock sample on rotating table, 2 = grinding wheel, 3 = water lubrication, 4 = pressurized air nozzle for sample removing water droplets from sample top surface, 5 = UV-light, 6 = normal light, 7 = camera taking pictures of sample with both UV and normal light.

Referring to the previously presented equipment of GRN16 grinding machine and its functionality, the machine gives solutions to problems presented by Pascual-Cebrian et al. (2013) as follows:

- Increased inter-section resolution by adjustable grinding thickness ultimately down to 1-micrometer level
- Increased grinding precision by a computer-controlled grinding system
- Constant lighting conditions during taking an image provided by integrated visible-light- and LED-UV-light lamps inside the grinding chamber
- Images are aligned automatically by using a special computer program instead of time-consuming manual alignment

Even though the 3D-grinder machine has made significant development in the application of the grinding tomography method in geosciences, the digitizing of features on images and 3D-modelling of microfractures is still a mostly manual and time-consuming process. For this reason, from the total of 600 images representing the 3,8 cm grinded thickness of the sample ORR-1.3.-2019, just 10 images with a fixed 0,42 cm image slice spacing were used in the 3D-analysis (Table 2).

Table 2. Z-coordinates of 10 images used in modelling of ORR-1.3-2019.

Image ID	3D-grinder Z-coordinate [cm]	Model Z-coordinate [cm]
1	1,6081	0
2	2,0319	0,4238
3	2,4557	0,8476
4	2,8795	1,2714
5	3,3033	1,6952
6	3,7271	2,119
7	4,1509	2,5428
8	4,5747	2,9666
9	4,9985	3,3904
10	5,4223	3,8142
	Image spacing [cm]:	0,4238

4.5.3. Modelling workflow of 3D-microfracture networks

After taking the tomography images using the GRN16 grinding machine, the next step was to continue with the processing of image dataset, followed by the 3D modelling workflow of microfractures.

As the grinder's horizontal camera positioning is not perfectly fixed during the experiment, the images had to be aligned to match the features and extents of the sample images in 3-dimensions (Fig. 16A). The alignment was done using Align app computer software programmed for the automatized processing of the GRN 16 grinding tomography data. After the alignment of the data, the sample had to be georeferenced for the definition of the location and orientation of the sample within the study area based on the information from the field notes and sample preparation (Fig. 16B). The georeferencing was done using the QGIS program's georeferencing tool.

After georeferencing, a set of 10 images were selected for the modelling, and z-position coordinates were defined for each image based on the information collected by the grinding machine (Fig. 16C). On each image, the microfractures were digitized using ArcGIS software with a similar workflow to macro-scale fracture digitizing from UAV and SLR photo-mosaics (Fig. 16D).

Now that the images and fractures had x, y, and z locations, the data was imported into Leapfrog geo 3D modelling software. The next step in software was to compare the layers of

images and fracture networks utilizing transparency and slice-section tools in order to recognize 3d geometry of the single fractures. After recognizing the continuous trace patterns through the z-dimension, polylines were drawn on each layer separately representing individual fractures (Fig. 16E).

After defining the fractures by drawing polylines on 2D traces continuing through z-direction, the polylines were imported into the Leapfrog geo software's "fault network" -function to interpolate the fracture surfaces based on the selected polylines (Fig. 16F). After the construction of fault surfaces, the cross-cutting and abutting relationships had to be defined for the mesh objects representing the fracture surfaces (Fig. 16G). Cross-cutting and abutting of single fault surfaces were interpreted based on the digitized 2D networks on tomography images.

The construction of a complete 3D microfracture network model was followed by an evaluation of structural data using Leapfrog geo's built-in tools (Fig. 16H), which creates evenly spaced virtual measurement points on the modelled fracture surfaces and evaluates structural orientations. After this, the data could be exported into the Leapfrog geo's stereonet tool for orientation analysis.

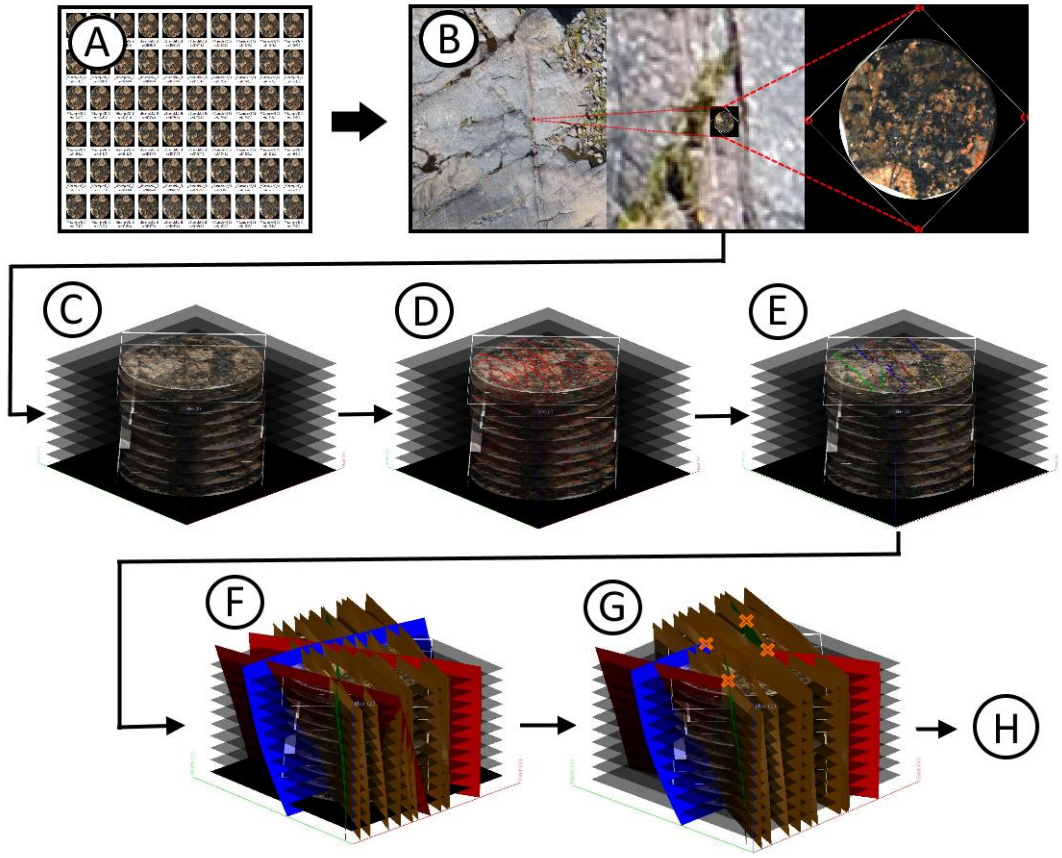

Fig. 16. Illustration of microfracture network modelling workflow on grinding tomography data. A: Automatic alignment of images using Align app -software. B: Georeferencing of images with their real

location and orientation using QGIS -software. C: Adding z-coordinate for images in Leapfrog geo 3D-modelling software. D: Digitizing of microfracture networks on images. E: Validation of fractures on different z-levels. F: 3D-modelling of microfractures based on validated 2D fracture polylines using interpolation functions of Leapfrog geo. G: Definition of interpreted abutting and cross-cutting relationships of modeled microfractures. H: Evaluation of structural data based on the interpolated fracture surfaces.

5. Modelling results and discussion

5.1. Scale 1 – UAV-orthophotography based 2D-modelling of fracture networks

Starting up with the UAV-scale fracture network data, the whole study area was subdivided into 6 structural domains based on the location of sinistral N-S trending faults and qualitatively evaluated spatial changes in fracture intensity. The domain division was inspired by subdivision approach of structural domains on the Island of Orrengrund conducted in Skyttä et al. (2021). The topological node (Fig. 17A) and branch (Fig. 17B) proportion analysis were conducted on each domain. In addition, a coarse overview of the strike orientation distribution of fractures and cumulative trace-length analysis was also made.

Based on the results, the highest deviation from average (full area) node and branch proportions towards increasing I-node and I-I-branch (terminating fractures) proportions are located within domains 1, 3, and 5, which are dominated by the poorly developed NNW-SSE trending regional fracture trend discussed by Skyttä et al. (2021). As we look at the node and branch proportions in domains 2, 4, and 6, we can see significantly increased proportions of Y-nodes and I-C (abutting fractures) and C-C branching (cross-cutting fractures) from the change of CB = 1,3 to CB = 1,4-1,6 (CB = average number of connections per branch), thus reflecting higher connectivity of the fracture network. As seen from the map, these domains are largely in line with the previously interpreted domains bound by N-S trending faults in Skyttä et al. (2021).

Increased fracture intensity on these domains is most likely associated with early-stage damage zones of the N-S trending faults and as well as with the wider dextral sensed linking damage zones, which kinematically connect the N-S trending faults (Skyttä et al. 2021). The topological data is supported by the rose-plot results (Fig. 17C), as the longest trace lengths are concentrated on the NE-SW trending set. The traces around the NW-SE trend, in turn, are vastly shorter in length, thus also implying higher connectivity due to abundant cross-cutting and abutting of fractures.

Power-law plots are suitable models for describing the distribution of fracture length, width (aperture), and displacements. However, according to Bonnet et al. (2001), fracture populations can exist where the distributions are followed by a lognormal or exponential distribution. Here we have a situation like this, as the trace length distribution seems to correlate with the exponential best-fit curve. This is common for the strata-bound systems, where the length distribution of joints depends on the nature of layering in rocks (Bonnet et

al. 2001). Similarly, as we have a heterogeneous fracture system on the Island of Orrengrund bound by major faults, such heterogeneities could be one reason suggested for explaining the exponential trace-length distribution in the study area.

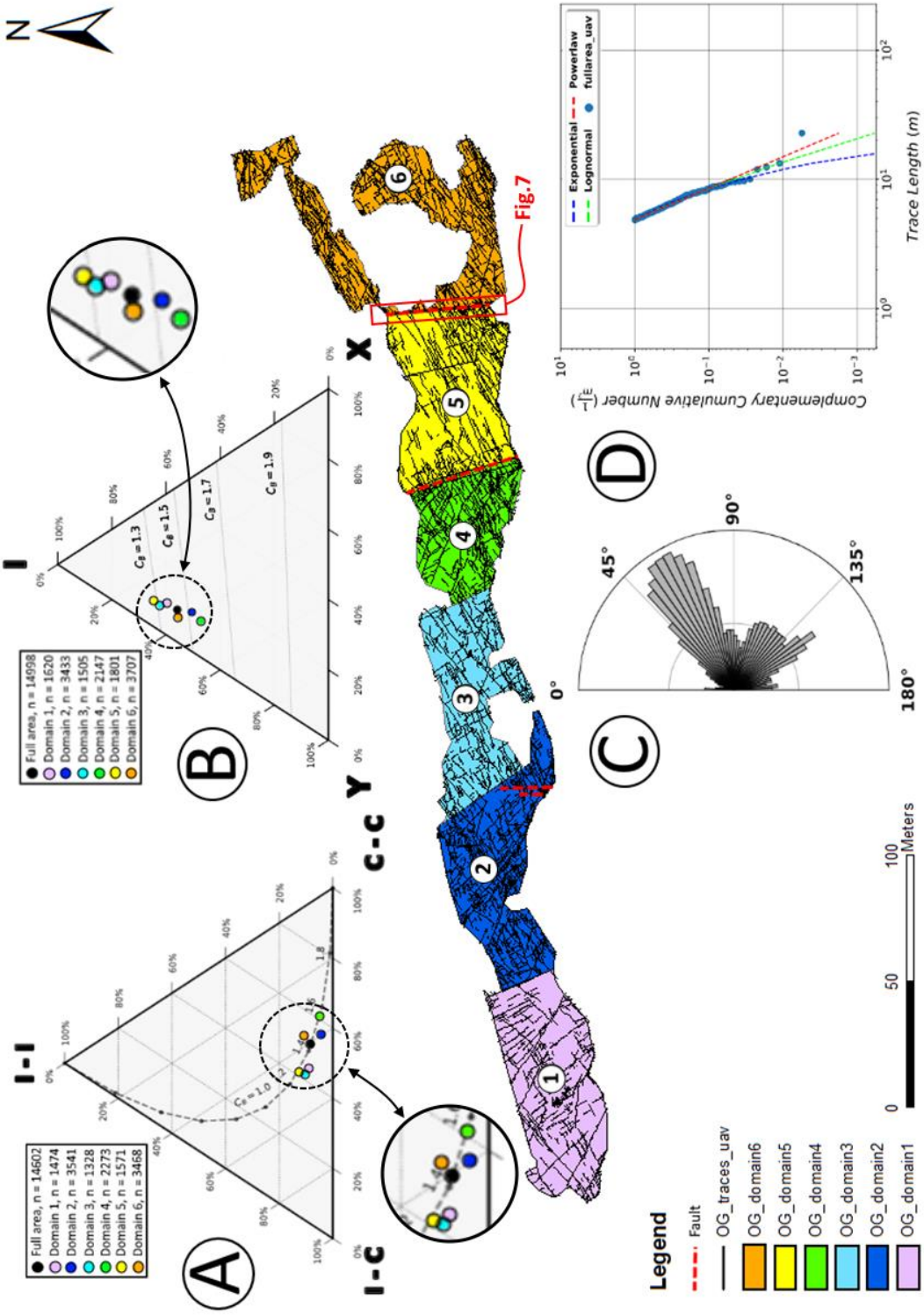

Fig. 17. Subdivision of UAV-scale fracture network into six structural domains for comparison of topological parameters. A: Plot showing the proportions of branches within domains. B: Plot showing the proportions of nodes within domains. C: Rose plot showing the orientation distribution of whole study area. D: Power-law plot of the trace lengths.

5.2. Scale 2 – SLR-orthophotography based 2D-modelling of sinistral fault

Joint measurements conducted on the field were divided into three sets of which the sub-vertical NE-SW (Fig. 18A and C; green) represents the poorly developed regional fracturing discussed in the previous chapter and in Skyttä et al. (2021). The second set covers the sub-vertical NNW-SSE fracture measurements, which represent the slip surfaces of the sinistral fault, thus here called as fault core. The third set is the WNW-ESE trending set with approximately 60-70 dip angle, which differs from the vertical-sub vertical dips of the background fracturing and fault core set.

By comparing the orientations of fractures in the neighbouring sinistral fault structure on the western side of the studied fault (Fig. 18B), the wing-crack type damage zone of the fault has the same orientation to the WNW-ESE set measurements. As the fractures in tip damage zones open in the perpendicular direction to major principal stress (Brace and Bombolakis, 1963; Lajtai, 1971) as mode I fracture, these structures can give some indication of the paleo-stress field when the faults were kinematically active. In other words, the WNW-ESE direction can represent the direction of principal stress in the paleo-stress field, as illustrated in Fig. 18B.

The fact that the WNW-ESE set has a dip angle deviating from the vertical to sub-vertical fault core and background fracturing is supporting the idea of the step-over style linking damage zones linking the N-S trending faults, thus the linking damage zone involves the formation of pop-up or pull-apart basins (Dooley and McClay 1997). In these basins, the local extension or compression creates a trans-tensional or -compressional mechanism, which results in secondary faulting with dip angles lower than 80-90-degrees.

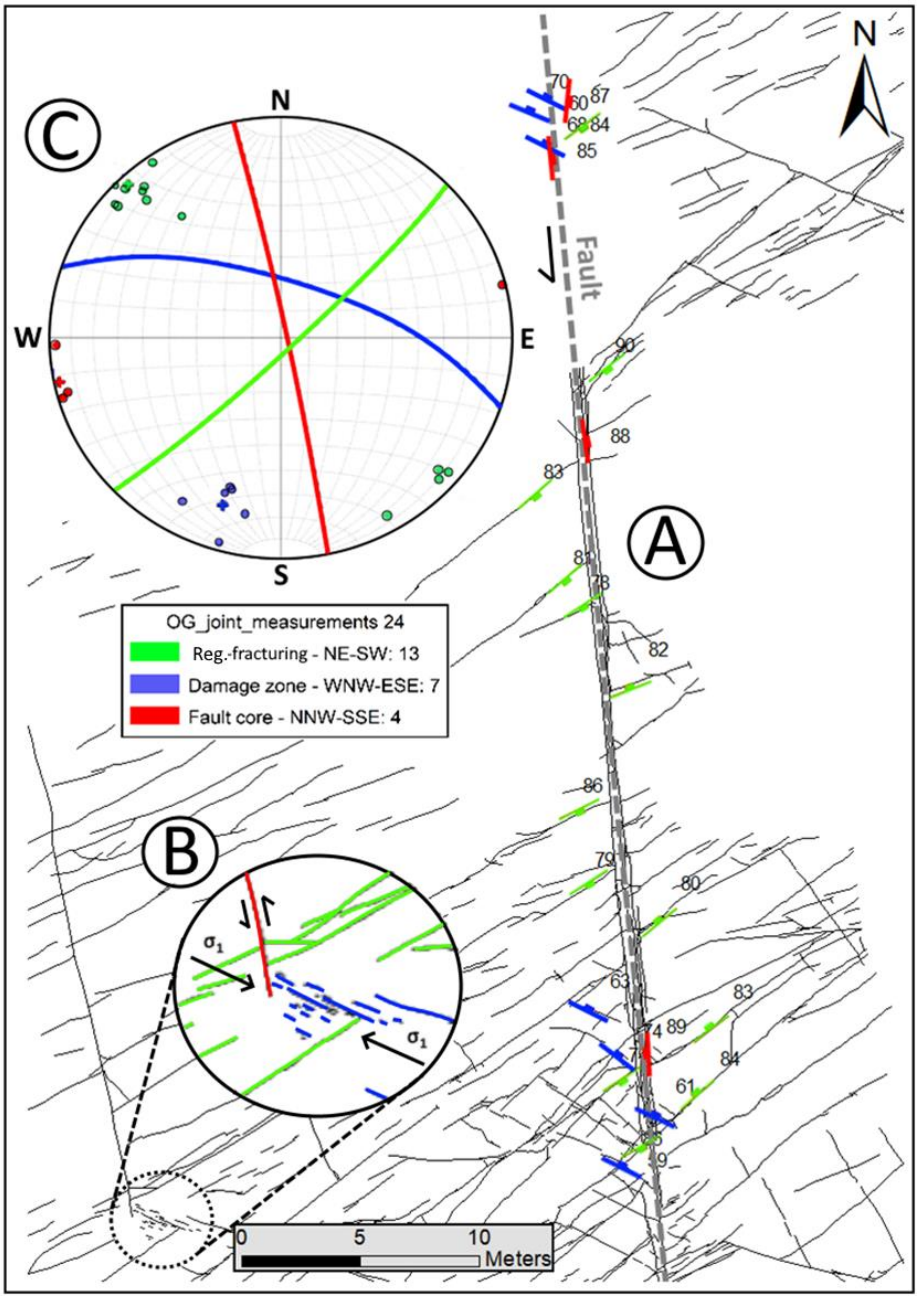

Fig. 18. Compass measurements of sinistral fault shown on UAV-fracture network (A) and lower hemisphere projection (=stereoplot) (C). The stereoplot presents orientation from three fracture sets (poles) including the mean plane for each set (great circle). The color coding is marked as follows: green = NE-SW trending regional fracturing, blue = WNW-ESE trending damage zone, and red = NNW-SSE trending fault core. Close-up of damage zone of neighboring fault structure (B) is also presented for correlation of relationships between fracture sets.

In the next analysis step, the scale of the fracture trace network was refined from scale 1 (UAV-scale) to scale 2 (SLR-scale). Fig. 19A shows the full SLR-scale fracture network of the studied sinistral fault. In order to compare the geometrical and topological properties of the fault, the network was subdivided into three zones with approximately 25 cm overlap on each side of the fault. The middle zone 3 represents either fault core, which is gradually changing into wall type damage zone in zone 2. Zone 1, in turn, represents the part of the damage zone where the fracture intensity is significantly lower, or regionally fractured rock outside the damage zone.

As predicted, the Y- and X-node proportions decrease with equal rate from zone 3 to zone 1, while the proportions of I-nodes increase. The same trend can be seen from the variation of CB values, where CB > 1,8 in fault core (zone 3), whereas the damage zone 2 has CB < 1,8. The damage zone 1, in turn, has a significant difference with CB ≈ 1,6. With both ternary plots, there is a gap between the results of damage zones 1 and 2. This observation highlights the localization of deformation within the damage zone, as the fracture intensity significantly lowers within 1 m of distance from the fault core, thus affecting to i.e. hydraulic properties of the rock mass in a relatively short range of distance.

Most of the fracture orientation sets recognized in the UAV-scale and SLR-scale rose-plots representing damage zone 1 (Fig. 19B) appear similar. However, as we move closer to the fault core (Fig. 19B; zones 2 and 3), the length of WNW-ESE damage zone fracturing, and NE-SW background fracturing significantly decreases during the kinematically synchronous formation of damage zone and abutment of the regional fractures at the continuous slip surfaces

Here again, the cumulative trace length plot shows distribution deviating from the power-law distribution towards the lognormal distribution, as seen from Fig. 19E.

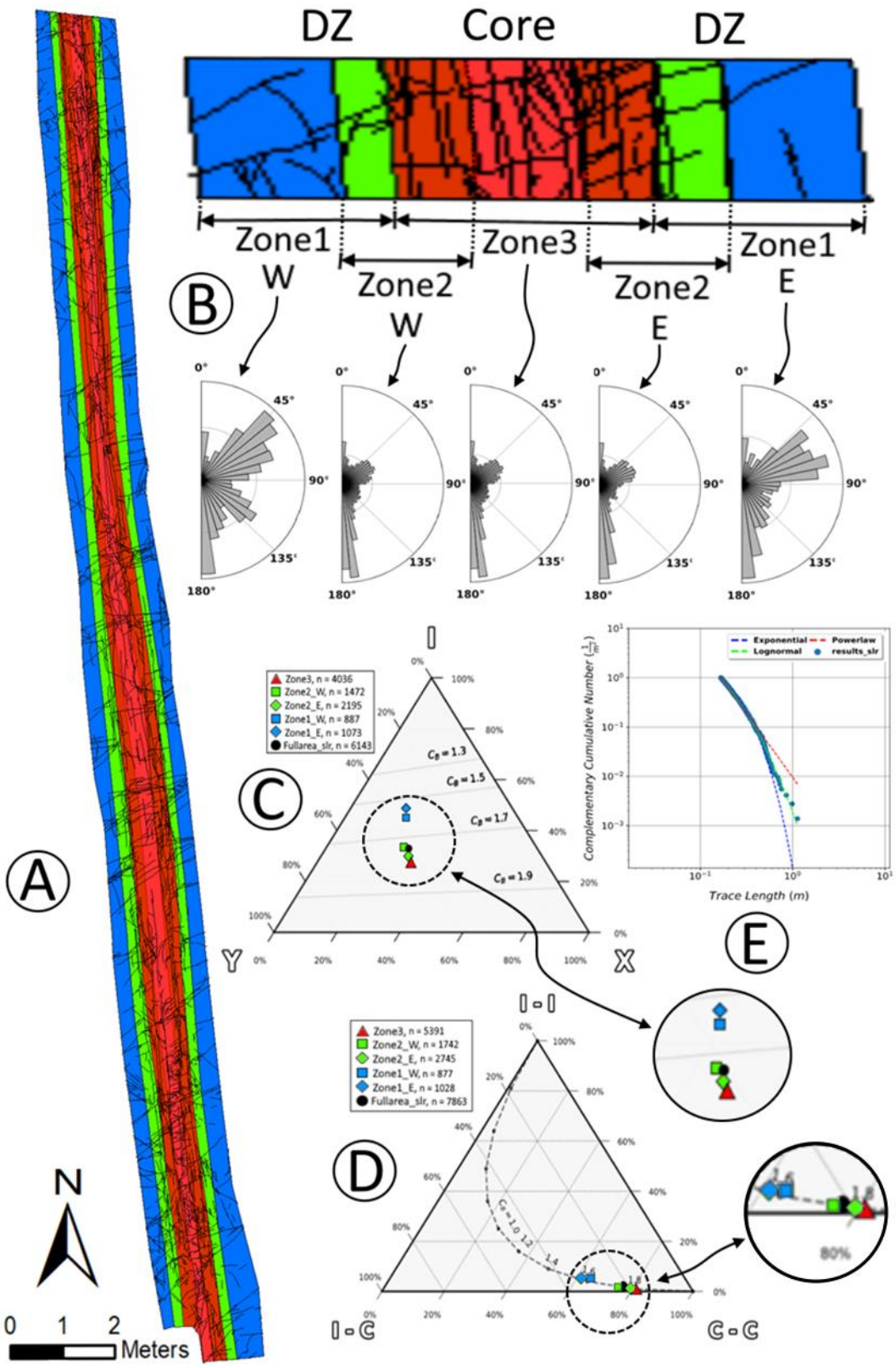

Fig. 19. Compilation of analysis results on SLR-scale fracture network on sinistral fault. A: Fracture network with selected core (red) and two damage zones (green and blue). B: Rose-plots showing the orientation distribution of fractures within core and damage zones. C: Plot showing the proportions of nodes within zones. D: Plot showing the proportions of branches within zones. E: Power-law plot of the trace lengths.

5.3. Comparison of fracture network analysis in UAV- and SLR-scales

Comparison of the scale 1 (UAV) and scale 2 (SLR) fracture trace data is presented in Figs. 20A-B, where we use the SLR-scale interpretation area as the boundary for comparison. It can be seen that the SLR-scale has a higher level of detail compared to UAV-scale, as the same interpretation area covers 7863 branches for SLR-scale, and for the UAV-scale the same area contains only 414 branches. Surprisingly, the node and branch proportion comparison show that both data sets have similar CB values with both node and branch plots, yet the UAV-scale has slightly higher amounts of Y-nodes than the SLR-scale. Also, it seems that both data sets can replicate the same sets of orientations well.

However, the cumulative trace length distribution seems to be problematic as the SLR-scale follows the lognormal distribution and UAV-scale exponential. Observations like this remind of the problem of the "scaling-up effect" discussed by i.e. Crider (2015). According to Crider (2015), "for the given ubiquity of inherited structures in crystalline rocks, fractal descriptions and scaling laws for faults are probably not relevant at length-scales smaller than the pre-existing flaw or precursory structure". This is partly why the modelling of the engineering- and crustal-scale processes in bedrock based on laboratory results alone can be difficult (Crider 2015).

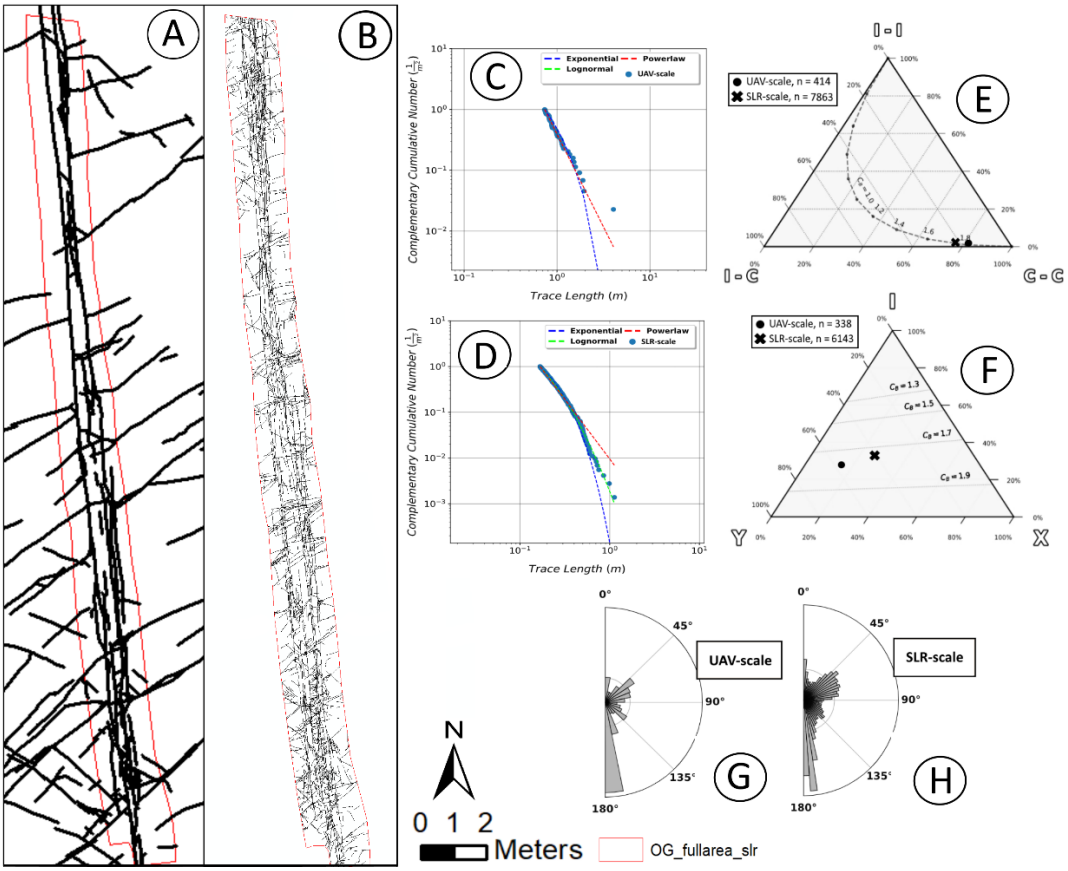

Fig. 20. Comparison of UAV- (A) and SLR-scale (B) fracture networks through differences in branch (E) and node (F) proportions, and deviation in power-law plots (C for SLR and D for UAV) and rose-plot orientation distributions (G and H).

5.4. Scale 3 – 3D-micro-tomography model of the sample ORR-1.3-2019

5.4.1. Structural setting of observed microfractures

Before the 3D modelling of the microfracture network in ORR-1.3-2019, the detailed grinding tomography images and digitized fracture traces were analysed for identifying the structural setting of observed microfractures. The fractures were mainly visible on light-red coloured K-feldspar phenocrysts, whereas there were difficulties to recognize microfractures from the dark-coloured matrix of the Rapakivi granite. However, the colour contrast between K-feldspar phenocrysts and matrix was useful for the observing the displacements in the sample.

The microfracturing in the sample seems to be mainly dominated by coincident grain boundary cracking discussed by Kranz (1983), where the fracture is created between the mineral grain and the matrix. The differing mechanical properties of the K-feldspar and plagioclase and hornblende bearing matrix play most likely a large role in the creation of micro-scale weakness zone on the boundary between the grain and the matrix, which allows cracking to propagate through the creation of inter-granular cracks (Fig. 21E; ii). As the weakness is in the grain boundary instead of the mineral structure itself, the coincident grain boundary cracks propagate parallel to grain boundary from grain to grain, as seen for example from Figure 21C, where fracture develops curvature controlled by the location of the orbicular K-feldspar grain within the matrix.

Non-coincident grain boundary cracking is also present mainly on round-shaped K-feldspar phenocrysts and occurs as typical microfractures striking through the centre of the K-feldspar phenocrysts. As the largest phenocryst grains are almost symmetrical in shape, the maximum internal tensile stress inside the grain is created perpendicular to the maximum compressive stress, thus the cracks form in a 90-degree angle to the grain boundary (Fig. 21E; i). The macroscopically isotropic character of the rock allows cracks to propagate in any direction depending on the stress field. Fig. 21E shows a typical example of a non-coincident micro-crack penetrating the K-feldspar phenocryst perpendicular to the grain boundary.

The dominating kinematic indicators observed from the sample were internal displacements in K-feldspar grains and micro-scale damage zone cracking. On the outcrop scale, the rock shows a sinistral sense. This is also supported by sinistral displacements within K-feldspar grain as presented in Fig. 21D. However, some of the micro-scale structures show also dextral sensed domains, like the extensional linking damage zone interpreted on the micro-crack traces (Fig. 21B; i) and displacements (Fig. 21B; ii) of the K-feldspar grains.

Fig. 21A also shows early-stage development of sinistral linking damage zone (Fig. 21A; ii) between two fractures (Fig. 21A; i) replicating the fault slip initiation mechanism discussed by Crider (2015) where fault slip is nucleated by the interaction of multiple micro-scale Mode-I tension cracks (Fig. 5a; i-iii). This observation of proto-shear fracture development is

remarkable as most of the observations on fracture kinematics are made on the fractures that had been already active.

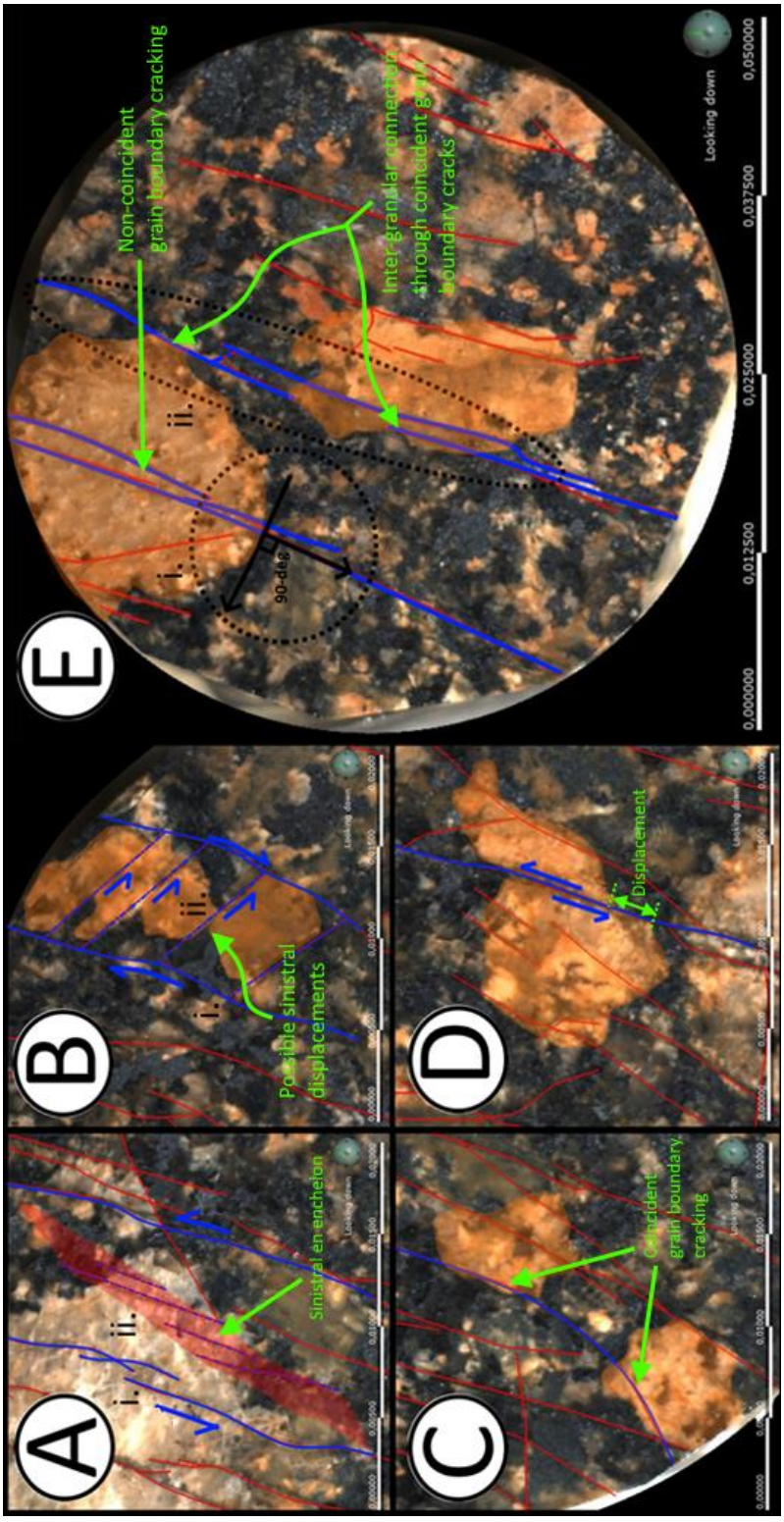

Fig. 21. Examples of morphological characteristic of fractures and kinematical indicators identified from grinding tomography images. Red lines represent digitized fractures on images and blue lines are highlighted fractures. Green arrows point out the described features. A: Sinistral development of damage fracture correlating with the model presented by Crider (2015). B: Possible dextral linking damage zone with rotation of grains. C: Coincident grain boundary cracking controlling the fracture propagation. D: Sinistral displacement of grains. E: Development of cracking through inter-granular connection of coincident grain boundary cracking. An example of non-coincident grain boundary cracking is also show in part E (highlighted with green arrow and description text).

5.4.2. Identification of fractures in 3-dimensions from grinding tomography data

11 of the total 16 modelled microfracture surfaces showed NNE-trends and sub-vertical dips (Fig. 22C). These fractures represent the slip-induced microfracturing occurring parallel with slip surface. Between the slip surfaces, slip-induced microfractures occur as NE-trending and sub-vertical dipping microfracture set (2 observed and modelled fractures) which abut the fault-parallel microfractures (Fig. 22E), and thus represent kinematically synchronous micro-scale damage fracturing. In addition, 2 pcs of NNW-trending sub-vertically dipping fractures (Fig. 22D) were modelled with a similar topological relationship to the principal fault-parallel microfractures. According to the digitized fracture traces, the NNW-trending microfracture set seems to terminate to a horizontal discontinuity not visible in the tomography images, as illustrated in Fig. 22D. Lastly, one moderately dipping fracture was observed perpendicular to the fault slip surface-parallel microfracturing (Fig. 22F). Unlike the other observed sets of microfractures, this set perpendicularly crosscuts multiple individual fault-parallel microfractures, thus unlikely representing damage fracturing kinematically linked to fault slip. The complete 3D-model is shown in Fig. 23.

Due to the sparse 0,42 cm image spacing, critical 3D information is lost between slices, thus making 3D interpretation of small fractures difficult. This applies especially to microfractures with a low dip-angle. In addition, most of the fractures were interpreted on the light-coloured K-feldspar grains, whereas fractures on the dark matrix were not clearly seen. For this reason, not all the fractures digitized can be observed on all z-levels of images. The resulting model is a simplified geological model, yet still having sufficient geological information to present the kinematics and topology of the microfracture network in the sample ORR-1.3.-2019.

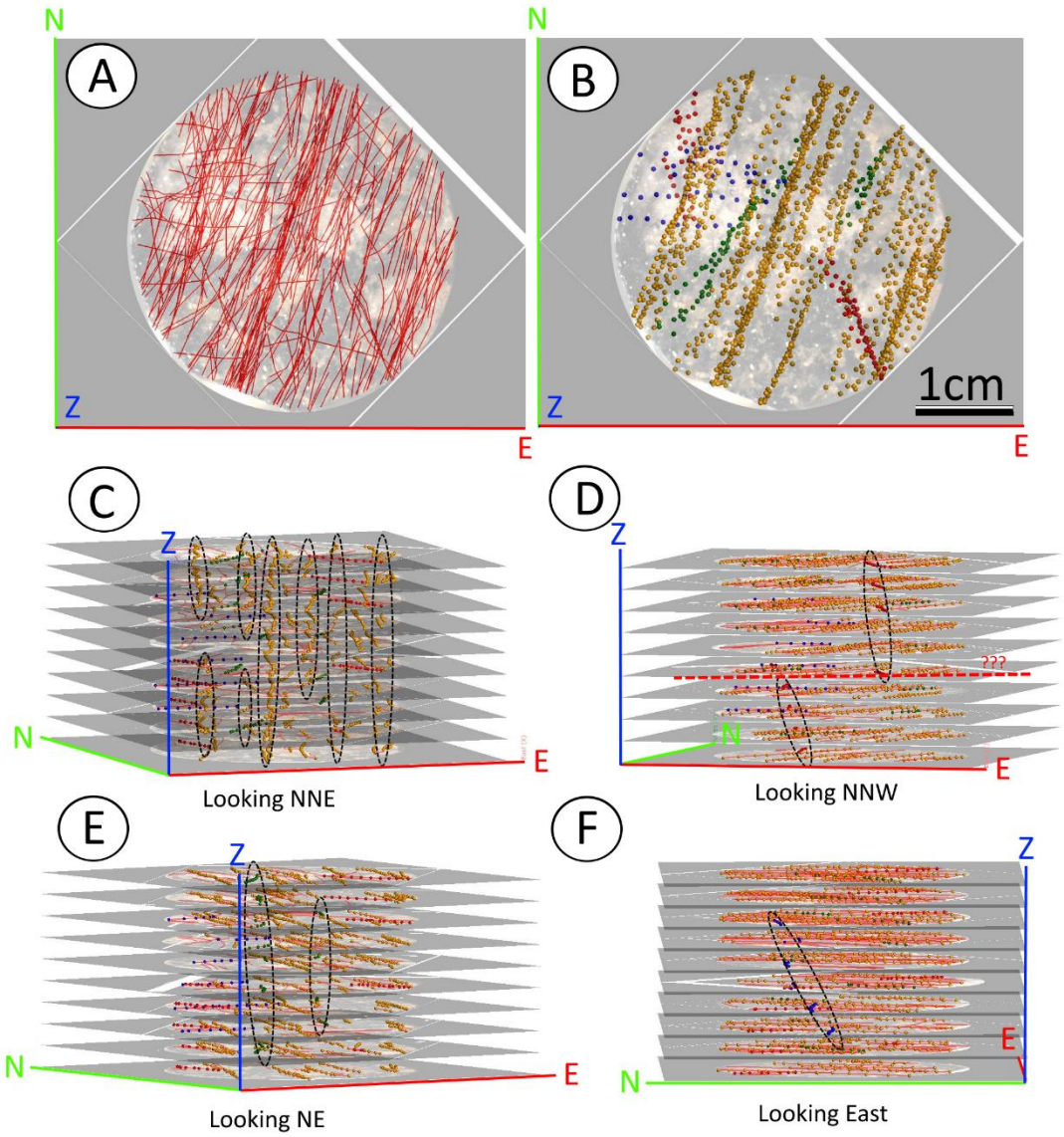

Fig. 22. A: Top view of the digitized fracture networks on all the 10 grinding tomography images shown in one figure. **B:** Polyline points representing the interpretation of individual fractures from the digitized fracture trace data. **C:** Identification of NNE-trending vertical fracture set. **D:** Identification of NNW-trending sub-vertical fracture set. **E:** Identification of NE-trending sub-vertical fracture set. **F:** Identification of steeply dipping East-trending fracture set.

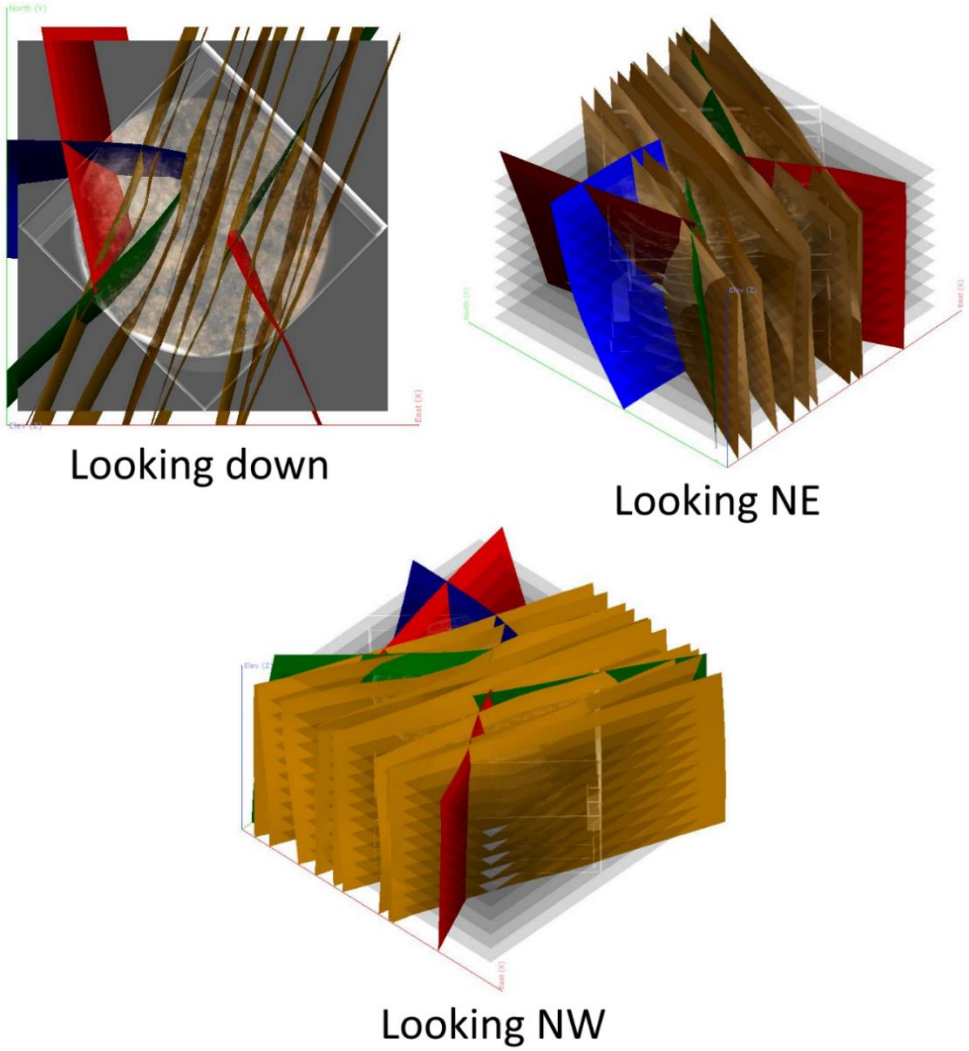

Fig. 23. Complete 3D model of microfracture system in ORR-1.3-2019. Modeled fractures are divided into four sets: Orange = NNE, Red = NNW, Green = NE, Blue = EW.

5.4.3. 3D-orientation of microfracture network

After the 3D modelling of microfracture networks in sample ORR-1.3.-2019, the orientation analysis was conducted on the modeled fracture surfaces by utilizing the structural geology functions of Leapfrog -software. In analysis, the virtual structural measurements were created on the mesh surfaces (fractures) after which the data could be imported into Leapfrog geo's structural data analysis tool. Virtual structural measurement counts are presented in Table 3.

Fig. 25A shows a stereoplot with compiled structural data of the modelled microfractures. The measurements are divided into four sets discussed in the previous chapter, which are presented as mean planes and poles on stereoplots (see compiled azimuths and dips in Table 3). By comparing the data in Fig. 25A with the outcrop field data presented in Fig. 25C the correlation of data is not clear. However, as we rotate the 3D model measurement data 45-degrees anti-clockwise (Fig. 25B), there appears perfect correlation with fracture set orientations between 3D-model measurements and outcrop measurements (Fig. 25B and C), thus revealing a large

error in the orientation of the 3D models orientation. The cause of the 45-degree azimuth error for georeferencing and later for structural measurements is still not clear. However, the most probable causes might have happened in the early stages, such as in sample preparation, in example when attaching the sample to the glass sheet.

The NNW-SSE -trending “fault core” fracture set presented in field measurements (Fig. 25C) has a slight deviation from the “fault slip set 1” azimuths measured from the 3D model (Fig. 25B). The 3D model measurements also reveal a new fracture set “fault slip set 2” appearing with sub-parallel orientation to “fault slip set 1”. However, the orientation of the “fault slip set 2” fractures are so close to “fault slip set 1” orientation, that they rather represent a part of the fault core than DZ tension fractures. The WNW-ESE -trending “damage zone” fracturing presented in Fig. 25C is also accurately replicated by “damage fracturing” set in a 3D model (Fig. 25B) with sub-vertical-vertical dip angles. In addition, the poorly developed NE-SW -trending regional fracturing set show a qualitatively good correlation in two data sets. Like in the field measurements, the regional fractures within the 3 3D-models of Scale 3 show sub-vertical to steep dips towards SE.

According to correlating results between the field and 3D model structural data, the fracture orientations in this sinistral fault at Orrengrund Island seems to be scalable from aerial scale down to the scale of the single mineral grain. With the qualitative overview of the model, it could be also said that the “3-dimensional topology” or “cross-cutting relationships” of the 3D model qualitatively matches with the observations made on the field. However, the 3D topology modelling on fracture networks is a topic that should be defined better and studied more in the future.

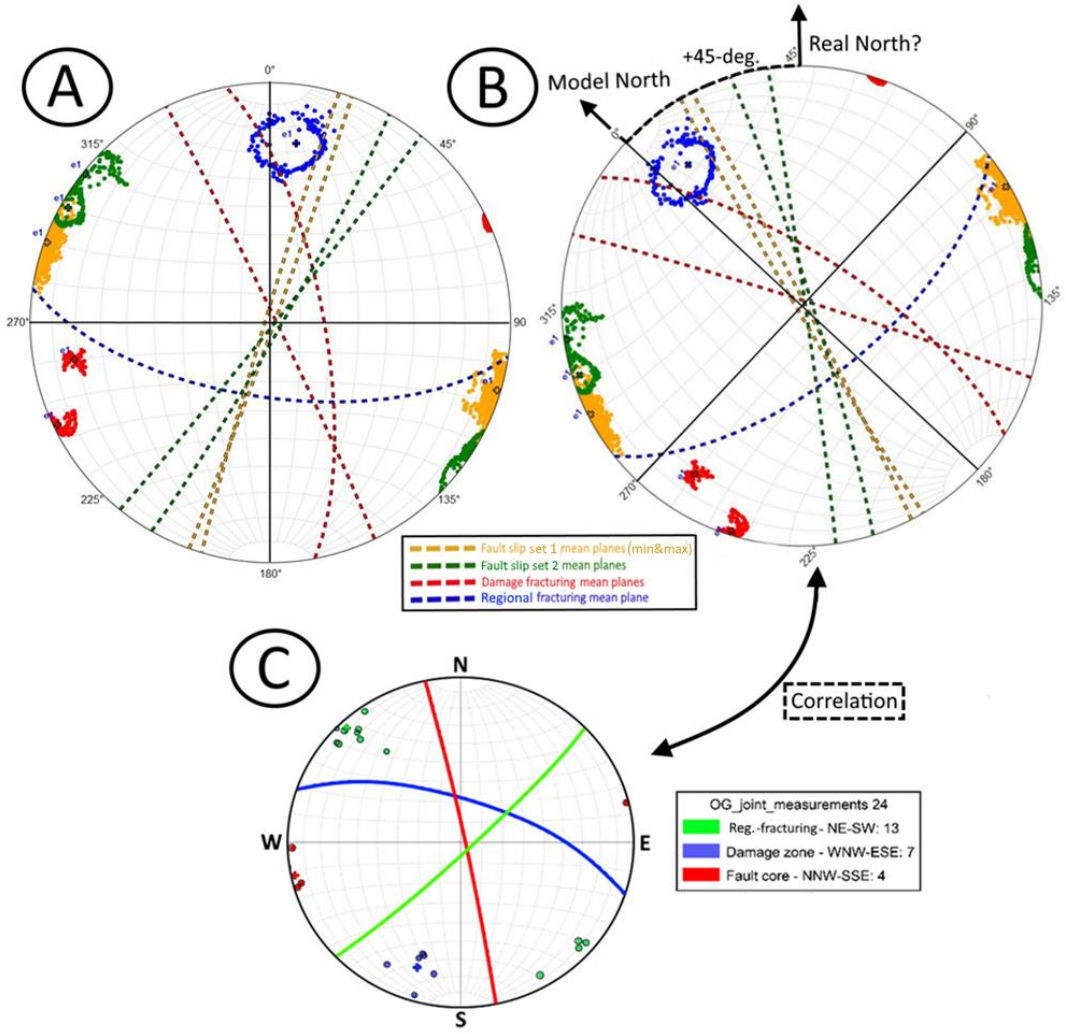

Fig. 25. A: Orientation distribution analysis based on virtual measurements done on modeled fractures. B: Orientation data rotated 45-degrees counter-clockwise to highlight the correlation of orientations with the outcrop measurements. These results show high possibility for error in sample preparation or oriented sampling done on field.

Table 3. Compilation of structural analysis results of modeled microfractures. The 45-degrees rotated azimuths are also presented. Colors in table represent the colors of fracture sets in Fig. 25.

Category	Virtual Surface Measurement Count N	Mean Dip [deg]	Mean Dip Dir. [deg]	45-Degrees Rotated Mean Dip Dir. [deg]
All data	5664,0	61,8	119,1	74,1
Set 1 – Fault slip set 1	3620,0	66,1	109,7	64,7
Set 2 – Fault slip set 2	933,0	66,7	124,6	79,6
Set 3 - Damage fracturing	702,0	71,0	76,7	76,7
Set 4 - Regional fracturing	359,0	64,5	188,1	143,1

6. Conclusions

I. GRN16 grinding machine solves multiple problems concerning the grinding tomography method in geosciences such as low resolution in inter-section space, poor grinding precision, poor lighting conditions, and missing of an automatic method for image alignment.

II. Refined SLR-data shows differing node and branch proportions and power-law analysis results compared to UAV-data of the same area most likely due to the scaling-up effect. However, the fracture orientations on both datasets correlate.

III. Microfracturing observed in Orrengrund rapakivi granite is controlled by coincident grain boundary cracking occurring on orbicular K-feldspar mineral grains boundaries or as non-coincident grain boundary cracking through the centre of grains. These factors allow cracks to propagate as inter-granular cracking from grain to grain and even bend cracks depending on grain's location.

IV. According to structural interpretation on tomography images of sample ORR-1.3.-2019, the sense of shear can vary on a micro-scale within one fault core, but is dominantly compatible with field observations.

V. ORR-1.3.-2019 dataset brought natural evidence of early-stage fault nucleation mechanism as discussed by Crider et al. (2015), where shear slip is created by the interaction of Mode I -cracking.

VI. Fracture orientation distributions measured on outcrop (also discussed in Skyttä et al. 2021) could be replicated using a 3D model based on a microtomography dataset produced with a 3D-grinder. Microfracture orientations correlate within the outcrop scale. In addition, 3-dimensional cross-cutting relationships (topology) of modelled fractures matched quantitatively with the outcrop scale observations.

7. Acknowledgements

First of all, I would like to thank the VYR (Valtion ydinjätehuoltorahasto) for funding of this master's thesis within the MIRA-3D project of the University of Turku. I would like to say a special thanks to my supervisor Prof. P. Skyttä for providing guidance and feedback throughout this MSc thesis project. Furthermore, I would like to thank N. Nordbäck from Geological survey of Finland for providing orthophotography data for this thesis. Thanks also to PhD student N. Ovaskainen for guiding me with the topology tools. In addition, I would like to thank MSc student J. Jokiniemi for collaboration and collection of the tomography image data used in this thesis. I also want to express my gratitude for the laboratory technician A. Peltola for helping me with sample preparation. Moreover, I would like to thank F. Xavier Gomez Coloma for collaboration and assistance with the 3D-grinder related computer software. Part of the results for this thesis was generated using Seequent Software. Copyright © Seequent Limited.

8. References

Aydin, A. 2000: Fractures, faults, and hydrocarbon entrapment, migration and flow. Marine and petroleum geology, 17(7), 797-814.

Bastesen E., Rotevatn, A. 2012: Evolution and structural style of relay zones in layered limestone-shale sequences: insights from the Hammam Faraun Fault Block, Suez rift, Egypt. Journal of the Geological Society, 169, 477-488.

Berkowitz, B. 2002: Characterizing flow and transport in fractured geological media: A review. Advances in water resources, 25(8-12), 861-884.

Billi, A., Salvini, F., & Storti, F. 2003: The damage zone-fault core transition in carbonate rocks: implications for fault growth, structure and permeability. Journal of Structural geology, 25(11), 1779-1794.

Bobet, A. 2000: The initiation of secondary cracks in compression. Engineering Fracture Mechanics, 66(2), 187-219.

Bonnet, E., Bour, O., Odling, N. E., Davy, P., Main, I., Cowie, P., & Berkowitz, B. 2001: Scaling of fracture systems in geological media. Reviews of geophysics, 39(3), 347-383.

Brace, W. F., Paulding Jr, B. W., & Scholz, C. H. 1966: Dilatancy in the fracture of crystalline rocks. Journal of Geophysical Research, 71(16), 3939-3953.

Brace, W.F., Bombolakis, E.G. 1963: A note on brittle crack growth in compression. Journal of Geophysical Research, 68(12), 3709-3713.

Brogi, A., Fabbrini, L., & Liotta, D. 2011: Sb–Hg ore deposit distribution controlled by brittle structures: the case of the Selvena mining district (Monte Amiata, Tuscany, Italy). Ore Geology Reviews, 41(1), 35-48.

Caine, J. S., Evans, J. P., & Forster, C. B. 1996: Fault zone architecture and permeability structure. Geology, 24(11), 1025-1028.

Chester, F. M., & Logan, J. M. 1986: Implications for mechanical properties of brittle faults from observations of the Punchbowl fault zone, California. Pure and applied geophysics, 124(1), 79-106.

Childs, C., Manzocchi, T., Walsh, J. J., Bonson, C. G., Nicol, A., & Schöpfer, M. P. 2009: A geometric model of fault zone and fault rock thickness variations. Journal of Structural Geology, 31(2), 117-127.

Choi, J. H., Edwards, P., Ko, K., & Kim, Y. S. 2016: Definition and classification of fault damage zones: A review and a new methodological approach. Earth-Science Reviews, 152, 70-87.

Chester, M., Chester, J.S. 2000: Stress and deformation along wavy frictional faults. Journal of Geophysical Research. 105, 23421-23430.

Cowie, P. A., & Scholz, C. H. 1992: Displacement-length scaling relationship for faults: data synthesis and discussion. Journal of Structural Geology, 14(10), 1149-1156.

Cloos, H. 1928: Über antithetische Bewegungen. Geologische Rundschau, 19, 246-251.

Crider, J. G. 2015: The initiation of brittle faults in crystalline rock. Journal of

Structural Geology, 77, 159-174.

Crider, J.G., Pollard, D.D. 1998: Fault linkage: Three-dimensional mechanical interaction between enchelon normal faults. Journal of Geophysical Research, 103, 24373-24391.

Crider, J. G., & Peacock, D. C. 2004: Initiation of brittle faults in the upper crust: a review of field observations. Journal of Structural Geology, 26(4), 691-707.

Choi, J-H., Edwards, P., Ko, K., Kim, Y-S. 2016: Definition and classification of fault damage zones: A review and a new methodological approach. Earth-Science Reviews, 152, 70-87.

Cox, S.F. 1999: Deformational controls on the dynamics of fluid flow in mesothermal gold systems. Geological Society, 155, 123-140.

Cruikshank, K.M., Zhao, G., Jhonson, A.M. 1991: Analysis of minor fractures associated with joints and faulted joints. Journal of Structural Geology, 13(8), 865-886.

Dooley, T., McClay, K. 1997: Analogue modelling of pull-apart basins. APPG Bulletin, 81, 1804-1826.

Dimmen, V., Rotevatn, A., Peacock, D.C.P., Nixon, C.W., Naerland, K. 2017: Quantifying structural controls on fluid flow: Insight from carbonate-hosted fault damage zones on the Maltese Islands. Journal of Structural Geology, 101, 43-57.

Dyskin, A. V., Germanovich, L. N., & Ustinov, K. B. 1999: A 3-D model of wing crack growth and interaction. Engineering Fracture Mechanics, 63(1), 81-110.

Engerlder, T., Hancock, P. 1989: Neotectonic joints. GSA Bulletin, 101(10), 1197-1208.

Forchhammer, F.A., Petterson, K., LaPointe, P., D-H, L. 2012: Geological discrete fracture network model for the Olkiluoto site, Eurajoki, Finland. Version 2.0. Posiva Technical Report-12-27.

Granier, T. 1985: Origin, damping, and pattern of development of faults in granite. Tectonics, 4(7), 721-737.

Hancock, J. W., & Thomson, R. D. 1985: Strain and stress concentrations in ductile fracture by void nucleation growth and coalescence. Materials science and technology, 1(9), 684-690.

Horii, H., & Nemat-Nasser, S. 1986: Brittle failure in compression: splitting faulting and brittle-ductile transition. Philosophical Transactions of the Royal Society of

London. Series A, Mathematical and Physical Sciences, 319(1549), 337-374. Ishii, E. 2016: Far-field stress dependency of the failure mode of damage-zone fractures in fault

zones: Results from laboratory tests and field observations of siliceous mudstone. Journal of Geophysical Research: Solid Earth, 121(1), 70-91.

Janecke, S. U., Dorsey, R. J., Steely, A. N., Kirby, S. M., Lutz, A., Housen, B. A., Forand, D. 2008: High geologic slip rates since Early Pleistocene initiation of the San Jacinto and San Felipe Fault zones in the San Andreas fault system, paper presented at Annual Meeting. South. Calif. Earthquake Cent., Palm Springs, Calif.

Kim, Y. S., Andrews, J. R., & Sanderson, D. J. 2001: Reactivated strike–slip faults: examples from north Cornwall, UK. Tectonophysics, 340(3-4), 173-194.

Kim, Y.S., Peacock, C.P., Sanderson D.J. 2004: Fault damage zones. Journal of Structural Geolgoy, 26, 503-517.

Kim, Y. S., & Sanderson, D. J. 2008: Earthquake and fault propagation, displacement and damage zones. Structural Geology: New Research, 1, 99-117.

Kranz, R. L. (1983): Microcracks in rocks: a review. Tectonophysics, 100(1-3), 449-480.

Kurt, H., Sorlien, C. C., Seeber, L., Steckler, M. S., Shillington, D. J., Cifci, G., Carton, H. 2013: Steady late quaternary slip rate on the Cinarcik section of the North Anatolian fault near Istanbul, Turkey. Geophysical Research Letters, 40(17), 4555-4559.

Lajtai, E. Z. 1971: A theoretical and experimental evaluation of the Griffith theory of brittle fracture. Tectonophysics, 11(2), 129-156.

Lopez, D.L., Smith, L. 1995: Fluid Flow in Fault Zones: Analysis of the Interplay of Convective Circulation and Topographically Driven Groundwater Flow. Water Resources Research, 31(6), 1489-1503.

Maerten, L., Gillespie, P., & Pollard, D. D. 2002: Effects of local stress perturbation on secondary fault development. Journal of Structural Geology, 24(1), 145-153.

Mattila, J., & Viola, G. 2014: New constraints on 1.7 Gyr of brittle tectonic evolution in southwestern Finland derived from a structural study at the site of a potential nuclear waste repository (Olkiluoto Island). Journal of Structural Geology, 67, 50-74.

Martel, S. J., & Boger, W. A. 1998: Geometry and mechanics of secondary fracturing around small three-dimensional faults in granitic rock. Journal of Geophysical Research: Solid Earth, 103(B9), 21299-21314.

Manzocchi, T. 2002: The connectivity of two-dimensional networks of spatially correlated fractures. Water Recourses Research, 38(9), 1-20.

Manda, A.K., Horsman, E. 2014: Fracturesis Jointis: Causes, Symptoms, and Treatment in Groundwater Communities. Groundwater, 53(6), 836-840.

McGrath, A.G., Davison, I. 1995: Damage zone geometry around fault tips. Journal of Structural Geology, 17(7), 1011-1024.

Mutlu, O., & Pollard, D. D. 2008: On the patterns of wing cracks along an outcrop scale flaw: A numerical modelling approach using complementarity. Journal of Geophysical Research: Solid Earth, 113(B6).

Nyberg, B., Nixon, C.W., Sanderson, D.J. 2018: NetworkGT: A GIS tool for geometric and topological analysis of two-dimensional fracture networks. Geosphere, 14(4), 1618-1634.

Nasseri, M. H. B., Rezanezhad, F., Young, R. P. 2011: Analysis of fracture damage zone in anisotropic granitic rock using 3D X-ray CT scanning techniques. Int J Fract, 168(1), 1-13.

Naylor, M. A., Mandl, G. T., & Supesteijn, C. H. K. 1986: Fault geometries in basement-induced wrench faulting under different initial stress states. Journal of structural geology, 8(7), 737-752.

Nironen, M. 1997: The Svecofennian Orogen: a tectonic model. Precambrian Research, 86(1-2), 21-44.

Ovaskainen, N. 2021: https://github.com/nialov/fractopo.

Pascual-Cebrian, E., Hennhöfer, D. K., & Götz, S. 2013: 3D morphometry of polyconitid rudist bivalves based on grinding tomography. Facies, 59(2), 347-358.

Peacock, D. C. P., Dimmen, V., Rotevatn, A., & Sanderson, D. J. 2017: A broader classification of damage zones. Journal of Structural Geology, 102, 179-192.

Peacock, D. C. P., Sanderson, D. J., & Rotevatn, A. 2018: Relationships between fractures. Journal of Structural Geology, 106, 41-53.

Petit, J. P., & Barquins, M. 1988: Can natural faults propagate under mode II conditions. Tectonics, 7(6), 1243-1256.

Rotevatn, A., & Fossen, H. 2011: Simulating the effect of subseismic fault tails and process zones in a siliciclastic reservoir analogue: Implications for aquifer support and trap definition. Marine and Petroleum Geology, 28(9), 1648-1662.

Rämö, O.T., Haapala, I. 1995: One hundred years of rapakivi granite. Mineralogy and Petrology, 52, 129-185.

Riedel, W. 1929: Zur Mechanik geologischer Brucherscheinungen ein Beitrag zum Problem der Fiederspatten. Geol. Palaont., 354-368.

Skyttä, P., Ovaskainen, N., Nordbäck, N., Engström, J., & Mattila, J. 2021: Fault induced mechanical anisotropy and its effects on fracture patterns in crystalline rocks. Journal of Structural Geology, 146, 104304.

Sanderson, D.J., Nixon, C.W. 2015: The use of topology in fracture network characterization. Journal of Structural geology, 72, 55-66.

Sylvester, A.G. 1988: Strike-slip faults. GSA Bulletin, 100, 1666-1703.

Scholz, C.H., Cowie, P.A. 1990: Determination of total strain from faulting using slip measurements. Nature, 346, 837-839.

Tchalenko, J. S. 1970: Similarities between shear zones of different magnitudes. Geological Society of America Bulletin, 81(6), 1625-1640.

Tchalenko, J. S., & Ambraseys, N. N. 1970: Structural analysis of the Dasht-e Bayaz (Iran) earthquake fractures. Geological Society of America Bulletin, 81(1), 41-60.

Vaasjoki, M., Rämö, O.T., Sakko, M. 1991: New U-Pb ages from the Wiborg rapakivi area: constraints on the temporal evolution of the rapakivi granite-anorthosite-diabase dyke association of southerastern Finland. Precambrian Research, 51(1-4), 227-243.

Viola, G., Mattila, J., Zwingmann, H., Todd, A., Raven, M. 2011: Structural and K/Ar Illite Geochronological Constraints on the Brittle Deformation History of the Olkiluoto Region, Southwest Finland. Posiva Working Report 2011-37.

Thiele, S. T., Grose, L., Samsu, A., Micklethwaite, S., Vollgger, S. A., & Cruden, A.

Woodcock, N. H., & Schubert, C. 1994: Continental strike-slip tectonics.In Continental deformation (pp. 251-263).

9. Attachments

ATTACHMENT 1: GRN16 operating manual for grinding tomography